

Supporting Information for:

**Design Principles for Trap-Free CsPbX<sub>3</sub> Nanocrystals:  
Enumerating and Eliminating Surface Halide Vacancies with Softer Lewis Bases**

David P. Nenon,<sup>†,⊥</sup> Kimo Pressler,<sup>†</sup> Jun Kang,<sup>⊥</sup> Brent A. Koscher,<sup>†,⊥</sup> Jacob H. Olshansky,<sup>†,⊥</sup>  
Wojciech T. Osowiecki,<sup>†,⊥</sup> Matthew A. Koc,<sup>†,⊥</sup> Lin-Wang Wang,<sup>⊥</sup> and A. Paul Alivisatos<sup>\*,†,⊥,§,#</sup>

<sup>†</sup>Department of Chemistry, <sup>#</sup>Department of Materials Science and Engineering, University of California, Berkeley, Berkeley, California 94720, United States

<sup>⊥</sup>Material Sciences Division, Lawrence Berkeley National Laboratory, Berkeley, California 94720, United States

<sup>§</sup>Kavli Energy NanoScience Institute, Berkeley, California 94720, United States

\*Author to whom correspondence should be addressed

<b>Additional experimental and computational details</b>	S3
<b>Additional discussion of surface termination models</b>	S6
<b>Additional details for the trapping model used to fit dilution experiments</b>	S8
<b>Step-by-step instructions for ligand exchange method</b>	S10
<b>Figure S1.</b> Calculated electronic structures of pristine CsPbCl <sub>3</sub> , CsPbBr <sub>3</sub> , and CsPbI <sub>3</sub>	S11
<b>Considerations for the design of future ligand systems</b>	S11
<b>Figure S2.</b> XPS results with fits for CsPbBr <sub>3</sub> nanocrystals	S12
<b>Table S1.</b> XPS results for four different CsPbBr <sub>3</sub> samples	S12
<b>Table S2.</b> Unweighted layer-by-layer composition of pristine CsPbBr <sub>3</sub> XPS samples	S14
<b>Table S3.</b> Weighted layer-by-layer composition of pristine CsPbBr <sub>3</sub> XPS samples	S15
<b>Figure S3.</b> <sup>1</sup> H NMR of oleylammonium iodide linewidth during dilution	S16
<b>Figure S4.</b> Binding isotherm for oleylammonium bromide ligands pairs	S17
<b>Figure S5.</b> GGA+PBE+SOC calculations of CsPbBr <sub>3</sub> +V <sub>Br</sub> and CsPbI <sub>3</sub> +V <sub>I</sub>	S18
<b>Figure S6.</b> Schematic of various ligand exchanges that can be performed	S19
<b>Figure S7.</b> Removal of surface ligands during ligand exchange	S20
<b>Figure S8.</b> Degradation product of amine/acid only ligand exchange	S21
<b>Figure S9.</b> Closer look at broad vs. sharp resonances of decylammonium and myristate	S22
<b>Figure S10.</b> <sup>1</sup> H NMR of oleylammonium–difluoroacetate ligand exchange	S23
<b>Figure S11.</b> <sup>1</sup> H NMR of oleylammonium–benzoate ligand exchange	S24
<b>Figure S12.</b> <sup>1</sup> H NMR of benzylammonium–oleate ligand exchange	S25
<b>Figure S13.</b> <sup>1</sup> H NMR of as-synthesized nanocrystals with impurities	S26
<b>Table S4.</b> Impurities in <sup>1</sup> H NMR of as-synthesized CsPbBr <sub>3</sub> nanocrystals	S26
<b>Figure S14.</b> Characterization of nanocrystals following purification	S27
<b>Figure S15.</b> PLQY and XRD evolution for 10x purification	S28
<b>Figure S16.</b> XRD of CsPbBr <sub>3</sub> nanocrystals purified with excess ligand	S29
<b>Figure S17.</b> DFT calculations of carboxylate anions	S30

<b>Table S5.</b> HOMO–LUMO energies for various carboxylates	S30
<b>Figure S18.</b> $^1\text{H}$ NMR NOESY spectra of ligand pairs without nanocrystals	S31
<b>Figure S19.</b> $^{31}\text{P}$ NMR evidence for binding of hexylphosphonate	S32
<b>Figure S20.</b> Quantification of Pb–difluoroacetate bonds by $^1\text{H}$ NMR	S33
<b>Figure S21.</b> Effect of native ligand concentration on PLQY	S35
<b>Figure S22.</b> Optical comparison of ligands with softer binding heads	S36
<b>Figure S23.</b> Optical comparison of carboxylates with variable chemical hardness	S37
<b>Figure S24.</b> Optical comparison of long and short fluorinated carboxylate ligands	S38
<b>Figure S25.</b> Effect of Z-type lead oleate on PLQY	S39
<b>Figure S26.</b> Investigation of nanowires and nanoplates	S40
<b>Figure S27.</b> Passivation efficacy across the visible spectrum	S41
<b>Figure S28.</b> Importance of CsX surface termination for optoelectronic performance	S42
<b>Figure S29.</b> Surface halide vacancies are present on facets, not edges/corners	S43
<b>Figure S30.</b> Optical properties of CsPbBr <sub>3</sub> nanocrystals with various ammonium ligands	S44
<b>Figure S31.</b> Trioctylphosphine oxide (TOPO) as a capping ligand	S45
<b>References</b>	S46

## Chemical Synthesis

### Preparation of Cesium Oleate Stock Solution.

A stock solution of cesium oleate was prepared following the reported procedure by Protesescu et al.<sup>1</sup> Briefly, 2.5 mmol  $\text{Cs}_2\text{CO}_3$  and 2.5 mL oleic acid was loaded into a three neck flask with 40 mL ODE, dried/degassed for 1 hour at 110 °C under vacuum, and then heated under dry Argon gas to 150 °C until all  $\text{Cs}_2\text{CO}_3$  reacted with oleic acid. The stock solution was stored in a glovebox.

### Synthesis of $\text{CsPbBr}_3$ Nanocrystals.

Anhydrous ODE (5 mL) and  $\text{PbBr}_2$  (0.188 mmol) were loaded into a 3-neck flask inside of a glovebox, and the flask was then transferred to a Schlenk line and dried/degassed under vacuum at 110°C for 15-20 minutes. Dried oleic acid (0.5 mL) and oleylamine (0.6 mL) were then injected under dry Argon gas and the temperature was raised to 140°C to complex the  $\text{PbBr}_2$  salt. Following complete dissolution of  $\text{PbBr}_2$ , which was found to occur within 15-20 minutes, the temperature was raised to 155°C for the injection of hot cesium oleate solution (0.5 mL, 0.125 M). The reaction mixture was cooled after 5 s using an ice-water bath.

### Isolation of $\text{CsPbBr}_3$ Nanocrystals.

Following the synthesis, 5-10 mL of anhydrous hexanes was added to the crude solution, which was then centrifuged at 4000 rpm for 3 min to remove excessively large nanocrystals and other unwanted byproducts. The supernatant should have a transparent, intense green color. The solubility of the nanocrystals now depends on the relative proportions of ODE, a poor solvent, and hexanes, a better solvent. By removing hexanes in a step-wise fashion using an argon or nitrogen line, different sizes of nanocrystals can be isolated from the same reaction mixture. We typically evaporated hexanes until the solution just started to turn cloudy, and then centrifuged at 10,000 rpm for 5 mins to isolate the nanocrystal population of interest. We usually found the first 1-2 precipitated fractions to have asymmetric linewidths and poor luminescence properties, and thus we typically discarded these fractions in favor of the higher-quality samples which precipitate as additional hexanes is removed.

### Synthesis of 2,2-difluorononanoic acid.

2,2-difluorononanoic acid was synthesized from ethyl iododifluoroacetate and 1-octadecene following a previously reported procedure.<sup>2-3</sup> Briefly, a mixture of  $\text{NiCl}_2 \cdot 6\text{H}_2\text{O}$  (0.2 g, 0.84 mmol), Zn dust (0.65 g, 10 mmol, Zn dust was HCl acid washed and dried prior to use), THF (10 mL), 1-octadecene (2.53 g, 10 mmol), ethyl iododifluoroacetate (1.3 g, 5 mmol), and 1 drop of water was stirred overnight at room temperature. Following purification by column chromatography (silica stationary phase with hexanes mobile phase), the expected ester, ethyl 2,2-difluorononanoate, was obtained. Next, a solution of ethyl 2,2-difluorononanoate (0.2 g, 0.625 mmol), lithium hydroxide (0.053 g, 1.26 mmol) in a 2:1 mixture of THF: $\text{H}_2\text{O}$  (5 mL) was stirred overnight at room temperature. The solvent was removed under vacuum and the residue acidified with 2% HCl, extracted with  $\text{CH}_2\text{Cl}_2$  (3 x 10 mL), washed with  $\text{H}_2\text{O}$  (3 x 10 mL) and dried ( $\text{MgSO}_4$ ). After removal of the solvent, recrystallization from acetone at low temperature yields the purified difluorinated acid product.

## **Experimental and Computational Details**

### **Nuclear Magnetic Resonance Spectroscopy (NMR).**

NMR spectra of micromolar concentrations of CsPbBr<sub>3</sub> NCs in deuterated toluene were measured on a Bruker 700 MHz instrument with an inverse cryoprobe for greatly enhanced <sup>1</sup>H sensitivity. Quantitative measurements were collected after tuning the probe and determining the exact 90° radio frequency pulse. After a spectrum was collected, concentration was determined by integrating the peak(s) of interest against an internal standard (mesitylene) of known concentration. 2D NOESY experiments were performed using a gradient-enhanced NOESY pulse sequence, with a mixing time of 500 ms and a delay time of 7 s. Spectra were typically collected overnight to ensure high-quality data. Once data was acquired, zero-filling and linear prediction were applied in the indirect dimension, then apodization functions of Sine Square 90° and Sine Bell 90° were applied – Sine Square in the direct dimension, and Sine Bell in the indirect dimension. Spectra were then manually phased and baselined to yield the final NOESY spectrum.

### **Optical Spectroscopy.**

All optical measurements were performed on dilute samples of nanocrystals in hexanes or toluene. For typical CsPbBr<sub>3</sub> nanocrystals, concentrations on the order of 1-10 nanomolar were found to have suitable optical densities. Absorption spectra were collected on a Shimadzu UV-3600 spectrophotometer with 0.5 nm increments using the slowest scan speed. Photoluminescence emission spectra were collected on a Horiba Jobin Yvon TRIAX 320 Fluorolog. Time-resolved fluorescence lifetimes were collected on a Picoquant Fluotime 300 with PMA 175 detector and an LDH-P-C-405 diode laser (excitation wavelength of 407.7 nm).

### **Absolute Quantum Yield Measurements.**

Absolute quantum yields were determined optically using a home-built integrating sphere spectrofluorometer. A Fianium SC450 supercontinuum pulsed laser is used as a white-light source. The desired excitation wavelength is selected using an excitation monochromator, and a small part of this excitation is directed to a ThorLabs S120VC calibrated silicon photodiode to measure the power, while the remainder is directed to a Spectralon integrating sphere from LabSphere, where it strikes a cylindrical cuvette containing the nanocrystal sample. The remaining light, which is a mixture of laser light and nanocrystal luminescence, eventually exits the integrating sphere and is focused onto an emission monochromator and the spectrum is detected using a thermoelectrically cooled Princeton Instruments PIXIS 400B CCD. The CCD is calibrated with a NIST-traceable radiometric calibration lamp. A complete description of our home-built integrating sphere spectrofluorometer can be found elsewhere.<sup>4</sup>

### **Powder X-ray diffraction (XRD).**

Diffraction patterns of drop-cast nanocrystal samples were obtained using a Bruker D-8 GADDS diffractometer equipped with a Co K $\alpha$  source and a Bruker Vantec 500 detector. Patterns were typically collected by merging frames centered at 2 $\theta$  = 30, 50, and 70 degrees where each frame was collected for 40 minutes.

### **Transmission Electron Microscopy (TEM).**

TEM images were obtained with a FEI Tecnai T20 equipped with a Gatan SC200 CCD camera and LaB<sub>6</sub> filament operated at 200 kV.

**X-ray Photoelectron Spectroscopy (XPS).** XPS spectra of CsPbBr<sub>3</sub> nanocrystals drop-cast on a Si wafer were collected using Thermo Scientific K-Alpha Plus X-ray photoelectron spectrometer. The spectra were acquired with monochromatized Al K $\alpha$  radiation and 400  $\mu$ m beam size. Cs, Pb, and Br were quantified by fitting GL(30) peak shapes and calibrating the C 1s edge to 284.8 eV.

### **Computational Methods.**

Density functional theory calculations were performed using the Vienna *ab initio* simulation package (VASP).<sup>5</sup> The core–valence interaction was described by the projector–augmented wave (PAW) method.<sup>6</sup> The cutoff for planewave expansion was set to 300 eV. Structures were relaxed until the force on each atom was smaller than 0.05 eV/Å. For the structural relaxation of systems with halide vacancies, the screened Coulomb hybrid functional of Heyd–Scuseria–Ernzerhof (HSE) was adopted,<sup>7</sup> and for the relaxation of other systems, the generalized gradient approximation of Perdew–Burke–Ernzerhof (GGA–PBE) was used.<sup>8</sup> The electronic structures for all systems considered were calculated at the HSE level after relaxation. The spin–orbit coupling (SOC) correction was also included in both structural relaxation and electronic structure calculations. The surface slab model was constructed based on orthorhombic CsPbX<sub>3</sub>. It contains 11 atomic layers in a 2 $\times$ 2 supercell with 216 atoms. A vacuum layer larger than 12 Å was used to avoid interaction between periodic images. The Brillouin zone was sampled by the  $\Gamma$  point.

Density functional theory calculations of carboxylate anions were performed using Gaussian software, the CAM-B3LYP hybrid exchange–correlation functional, a 631G++(d,p) basis set, and GD3BJ empirical dispersions.

## Additional discussion of surface termination models.

Understanding the relationship between nanocrystal surface chemistry and optoelectronic performance depends critically on an accurate model of the surface, which first requires the correct choice of surface termination. For low-index surfaces of  $\text{CsPbX}_3$  nanocrystals, three main surface termination models have been proposed:

1.  $\text{CsX}$  facet termination
2.  $\text{PbX}_2$  facet termination
3.  $\text{PbX}_2$  adlayer on  $\text{CsX}$  termination

$\text{CsX}$  termination is well-supported in the literature, and ultimately, we also find it to be the most plausible choice. We arrived at this choice by first constructing an atomic model for each case that is able to reproduce the measured XPS stoichiometry, and then considering the relative merits of each surface structure in light of existing experimental and theoretical results.

Briefly, layer-by-layer atomic models were constructed, each accounting for the different types of surface termination. Next, an exponential weighting term was applied to each layer based on its relative proximity to the surface, given that XPS is a surface-sensitive technique. Table S2-S3 contains an example for predicting the measured XPS stoichiometry of a pristine,  $\text{CsBr}$  terminated 9.4 nm  $\text{CsPbBr}_3$  nanocrystal. A brief description of each model can be found below for  $\text{CsPbBr}_3$ :

$\text{CsBr}$  termination:

- Pristine  $\text{CsBr}$  termination cannot produce measured XPS stoichiometry, but  $\text{CsBr}$  termination with both Cs and Br vacancies can. Specifically, ~60% of surface Cs and ~80% of surface Br must be vacant to yield the measured XPS signal

$\text{PbBr}_2$  termination:

- Pristine  $\text{PbBr}_2$  termination produces measured Cs:Pb ratio, but predicted Pb:Br ratio is smaller than measured. This can be accounted for with ligation of the surface by oleylammonium bromide ligand pairs. Specifically, ligation of ~35% of the surface produces the measured XPS signal. No Cs vacancies or Br vacancies are present

$\text{CsBr}$  termination with  $\text{PbX}_2$  adlayer:

- Removal of ~35% of surface Cs and ~12% of surface Br from  $\text{CsBr}$  layer, plus coverage of ~55% of the surface with  $\text{PbBr}_2$  species, is able to produce measured XPS signal

$\text{PbBr}_2$  termination can be ruled out. This model does not allow for oleylammonium substitution into Cs sites,<sup>9</sup> it produces a highly localized valence band maximum (Figure S28) that is inconsistent with 80-90% PLQY, and we have shown that the introduction of 5-fold coordinated lead atoms, such as the ones on this surface, have a detrimental effect on PLQY. Only 35% of the surface can be ligated with oleylammonium bromide pairs before the measured XPS signal is no longer produced, which means that each nanocrystal would have ~1000 trap states remaining after ligation. Again, this is inconsistent with high 80-90% PLQY. Additionally, *ab initio* calculations have determined this facet to have a less favorable formation energy than  $\text{CsBr}$  facets.<sup>10</sup>

$\text{CsBr}$  termination with a  $\text{PbBr}_2$  adlayer is promising in that it is able to produce the measured XPS signal while also accounting for oleylammonium substitution into Cs vacancies as well as ~12% of surface Br being vacant, a value we determined with  $^1\text{H}$  NMR and supported with

a simple trapping model. However, the structural validity of this model is arguable.  $\text{PbBr}_2$  species are charge neutral, making them unlikely to bind to a charge neutral  $\text{CsBr}$  facet unless a very strong bonding interaction is present, which is not the case in lead halide perovskite materials. Additionally, we identify a critical inconsistency between this surface model and the experimental results we present in the main text. We demonstrated that  $\text{CsPbBr}_3$  nanocrystals maintain relatively high (>50%) PLQY values despite the introduction of hundreds of surface halide vacancies, which was supported by *ab initio* calculations that revealed a shallow, delocalized defect level. However, *ab initio* calculations of this  $\text{CsBr}$  facet with a  $\text{PbBr}_2$  partial adlayer have shown that bromide vacancies introduce deep trap levels in this system. It is highly unlikely that  $\text{CsPbBr}_3$  nanocrystals could maintain PLQY >50% in the presence of hundreds of deep trap states. A similar argument can be made for the analogous surface in  $\text{CsPbI}_3$  materials. *Ab initio* calculations have shown that an iodide vacancy on this surface produces a deep trap level directly in the middle of the bandgap.<sup>11</sup> Again, it is extremely unlikely that  $\text{CsPbI}_3$  nanocrystals could maintain PLQY within measurement error (2-3%) of unity with the presence of hundreds of deep trap states on the surface. For both structural and electronic reasons, we thus conclude that  $\text{CsX}$  termination with a partial  $\text{PbX}_2$  adlayer is also not a plausible surface model.

This leaves  $\text{CsBr}$  termination as the most plausible surface model. This is the lowest energy facet of the three options,<sup>10</sup> the analogous  $\text{CH}_3\text{NH}_3\text{Br}$  facet of  $\text{CH}_3\text{NH}_3\text{Br}_3$  has been directly observed by scanning tunneling microscopy,<sup>12</sup> and it allows for the substitution of oleylammonium ions into Cs vacancies.<sup>9</sup> Additionally, *ab initio* calculations have demonstrated that halide vacancies on the surface of  $\text{CsCl}_3$ ,  $\text{CsPbBr}_3$ , and  $\text{CsPbI}_3$  terminated by  $\text{CsX}$  facets create trap levels of varying depths, which is in excellent agreement with the experimental results presented in the main text. The only potential inconsistency we were able to identify with this model is that in order to produce the measured XPS stoichiometry, ~90% of surface halide sites must be vacant, which does not agree with the  $^1\text{H}$  NMR determination of ~12% of surface halide sites being vacant. However, as stated in the main text, the number of halide vacancies determined by XPS represents an upper bound, as these radiation-sensitive materials are known to lose atoms, particularly halides, when exposed to high-energy sources in ultra-high vacuum conditions.<sup>13-14</sup> As such, we conclude that as-synthesized  $\text{CsPbX}_3$  nanocrystals are terminated by  $\text{CsX}$  facets, with both Cs and X vacancies present. Cs vacancies represent a more substantial fraction of the surface than do X vacancies, which yields a net negative charge that can be offset to neutral by the substitution of oleylammonium ions into Cs vacancies.

## A simple charge trapping model for PLQY vs. nanocrystal concentration.

Photoluminescence quantum yield (*PLQY*) can be expressed as a competition of rates.

$$PLQY = \frac{k_r}{k_r + N_{trap}k_{nr,trap}}$$

where  $k_r$  is the radiative rate,  $N_{trap}$  is the number of traps, and  $k_{nr,trap}$  is the effective nonradiative rate per trap, which here we assume to be constant. Alternatively, *PLQY* can be expressed in terms in terms of the ratio of the radiative and nonradiative rates.

$$PLQY = \frac{\frac{k_r}{k_{nr,trap}}}{\frac{k_r}{k_{nr,trap}} + N_{trap}} = 1 - \frac{N_{trap}}{\frac{k_r}{k_{nr,trap}} + N_{trap}}$$

Thus, an expression for  $N_{trap}$  would allow this equation to be used to fit the data in Figure 1 of the main text with  $k_r/k_{nr,trap}$  as the only fitting parameter. We adopted the Langmuir isotherm to develop an expression for  $N_{trap}$ .

$$\theta = \frac{K_{eq}[RNH_3^+X^-]}{1 + K_{eq}[RNH_3^+X^-]}$$

$$\theta = 1 - \frac{N_{trap}}{N_{max}}$$

where  $\theta$  is the fractional surface coverage,  $N_{max}$  is the maximum number of surface traps per nanocrystal (i.e. the number of surface halides per nanocrystal),  $K_{eq}$  is the free vs. bound equilibrium constant for oleylammonium halide ligand pairs, and  $[RNH_3^+X^-]$  is the mM concentration of oleylammonium halide ligands pairs free in solution. Combining these two expressions for  $\theta$  yields:

$$N_{trap} = \frac{N_{max}}{1 + K_{eq}[RNH_3^+X^-]}$$

$K_{eq}$  was determined to be 10.5 mM<sup>-1</sup> for oleylammonium bromide (Figure S4). Because anion exchange experiments have shown no preference for one halide ligand over the other,<sup>15-17</sup> we assumed that 10.5 mM<sup>-1</sup> is also applicable to oleylammonium chloride and oleylammonium iodide.  $[RNH_3^+X^-]_{free}$  can be determined by subtracting the number of bound ligand pairs from the number of total ligand pairs.

$$[RNH_3^+X^-]_{free} = [RNH_3^+X^-]_{total} - [RNH_3^+X^-]_{bound}$$

It is useful to express all relevant concentration in terms of the nanocrystal concentration,  $[CsPbX_3]$ , as this is the x-axis that is used for the fitting.  $N_{total}$  is the total number of ligand pairs per nanocrystal.



$$[RNH_3^+X^-]_{total} = [CsPbX_3]N_{total}$$

$$[RNH_3^+X^-]_{free} = [CsPbX_3]N_{total} - [CsPbX_3]N_{max} + [CsPbX_3]N_{trap}$$

$$[RNH_3^+X^-]_{free} = [CsPbX_3](N_{total} - N_{max} + N_{trap})$$

where  $[CsPbX_3]$  is the mM nanocrystal concentration. This expression can be substituted into the above expression for  $N_{trap}$  and expressed as a quadratic function.

$$K_{eq}[CsPbX_3]N_{trap}^2 + (K_{eq}[CsPbX_3]N_{total} - K_{eq}[CsPbX_3]N_{max} + 1)N_{trap} - N_{max} = 0$$

Completing the square to solve for  $N_{trap}$  yields

$$N_{trap} = \sqrt{\frac{(K_{eq}[CsPbX_3]N_{total} - K_{eq}[CsPbX_3]N_{max} + 1)^2}{4K_{eq}[CsPbX_3]} - N_{max}} - \frac{K_{eq}[CsPbX_3]}{K_{eq}[CsPbX_3]N_{total} - K_{eq}[CsPbX_3]N_{max} + 1}$$

$N_{trap}$  can now be calculated in terms of known experimental parameters plus the variable nanocrystal concentration, and used with the PLQY expressions above to fit PLQY vs. nanocrystal concentration and thus determine  $k_r/k_{nr,trap}$ , which describes the defect tolerance of these materials relative to each other.

Parameter	Determined Value
$N_{max}$	1537
$K_{eq}$ (mM <sup>-1</sup> )	10.5
$N_{total}$	6000

## Ligand Exchange Method

The following is a step-by-step description of the ligand exchange method introduced in the main text. We hope the additional level of detail here will help the reader achieve their desired results.

1. Select a nanocrystal sample to be exchanged
2. Determine nanocrystal edge length and concentration from absorption<sup>18</sup> and emission<sup>15</sup> spectra
3. Use edge length and concentration to calculate the appropriate concentration for exchange solution. We have found that excess ligand (roughly more than  $\sim 5$  ion pairs per  $\text{nm}^2$  of nanocrystal surface) risks partial transformation to the  $\text{Cs}_4\text{PbBr}_6$  phase (Figure S16)
4. Prepare an appropriate volume of the resuspension solution with concentration calculated above. To 3x exchange a 1 mL sample, at least 3 mL of resuspension solution is needed
5. Add a known volume of nanocrystal stock solution to a centrifuge tube
6. Add 2x the known volume of antisolvent (e.g. anhydrous ethyl acetate), e.g. 2 mL of ethyl acetate for a 1 mL nanocrystal solution in toluene/hexanes. Anhydrous antisolvents are important for achieving high optical performance, as bench antisolvents inevitably contain water
7. Centrifuge at 10,000 rpm for 5-10 minutes, ideally at low temperatures
8. Remove the centrifuge tube and gently invert, as to separate the pellet from the supernatant. We observed pellets of  $\text{CsPbBr}_3$  to break upon agitation, which is not desirable. If samples are going back into a glovebox, pumping them in upside down is essential to preserve the pellet
9. Discard the supernatant and resuspend the pellet with resuspension solution. Vortexing is often helpful to aid resuspension. We typically used the same volume as was initially present such that nanocrystal concentration is essentially unchanged, and thus the critical factor of ion pairs per  $\text{nm}^2$  is also essentially unchanged
10. Repeat steps 6-10 two more times to constitute a complete ligand exchange or purification. Anything that originally existed from the synthesis should be removed by this point
11. Finally, centrifuge the final resuspended solution at 10,000 rpm for 10 minutes. We typically observed a small precipitate, no larger than a pencil tip, which is likely comprised of aggregates that inevitably will occur during the precipitation and resuspension of nanocrystals with dynamic ligands. This step is especially important if the resulting solution will be used to make nanocrystal films, as aggregates degrade overall film quality. Note that care must be taken to remove the desired product, i.e. the solution, without disturbing the small precipitate. We found gentle removal of the liquid with a pipet to be effective

With regard to performing the ligand exchange in the glovebox versus on the bench, we typically chose to use fresh glovebox solvents, chemicals, and nanocrystal samples, but the actual exchange was performed on the bench. The use of glovebox chemicals minimizes the amount of water that is present, which is well known to be important for avoiding degradation of lead halide perovskite nanocrystals. Oxygen is less of a concern, hence our choice to perform most exchanges on the bench. Centrifuges and optical spectroscopies are all benchtop instruments.

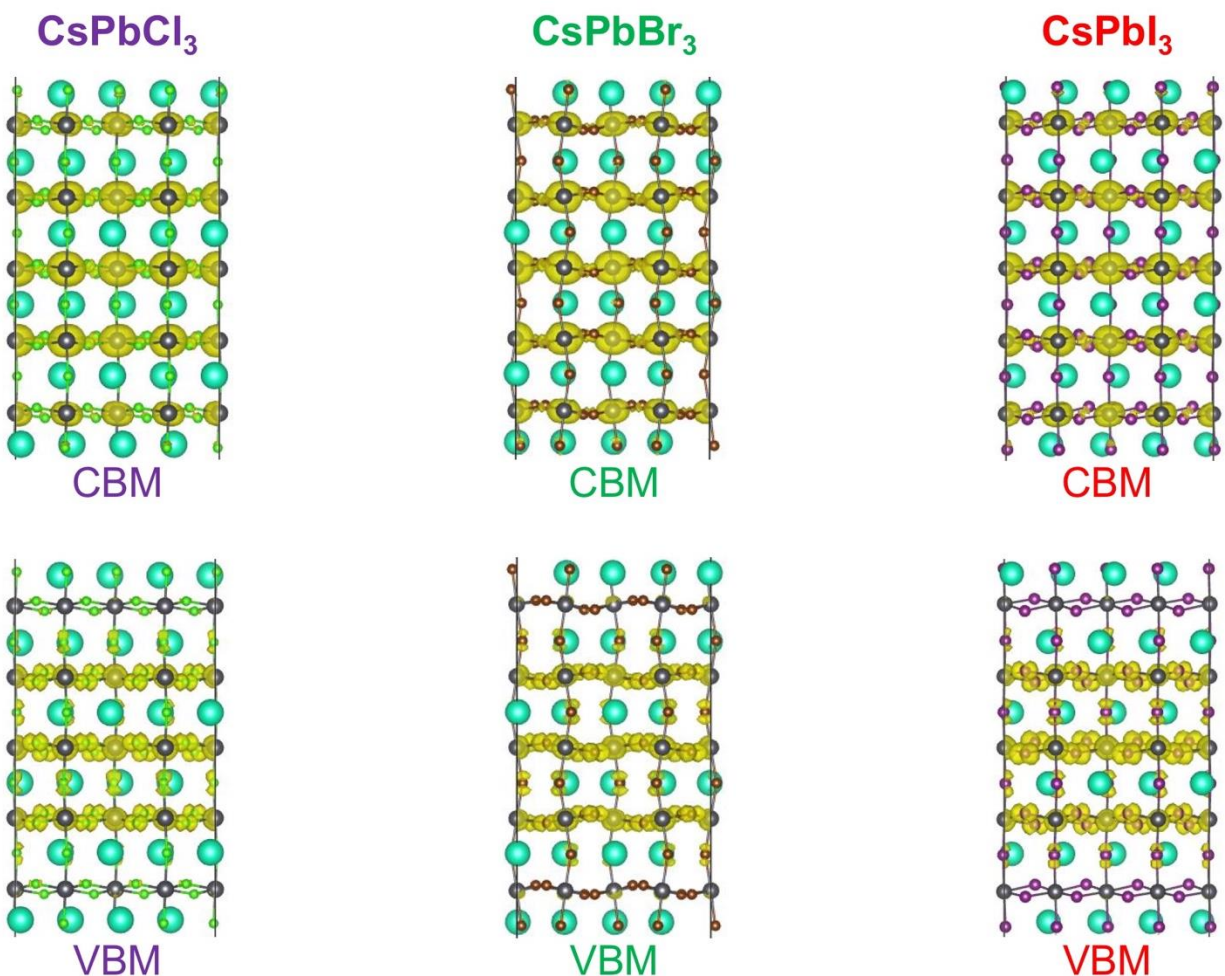


**Figure S1.** Electronic structure calculations for pristine  $\text{CsPbX}_3$  perovskite crystals terminated by  $\text{CsX}$  facets. These materials possess trap-free, fully delocalized electronic states without the need for any passivating ligands. This suggests that surface Cs and X dangling bond states lie outside of the bandgap and thus do not harm luminescence efficiency.

#### **Considerations for the design of future ligand systems.**

The observation that halide dangling bonds do not lie inside the bandgap has important implications for the design of future ligand systems. From a PLQY perspective, there is no need to passivate surface atoms that do not introduce midgap states, i.e. there is no need to passivate surface halides in these nanocrystals. Thus, the binding of oleylammonium to surface halides does not improve PLQY. In contrast, it actually tends to harm PLQY by removing surface halides, which introduces trap states. Surface halides can be removed either by the facile desorption of oleylammonium halide ligand pairs, or by the formation of volatile HX mineral acids following a proton transfer from oleylammonium. For these reasons, we believe the design of future ligand systems should avoid cationic species such as oleylammonium, as they tend to remove surface halides and thus decrease PLQY.

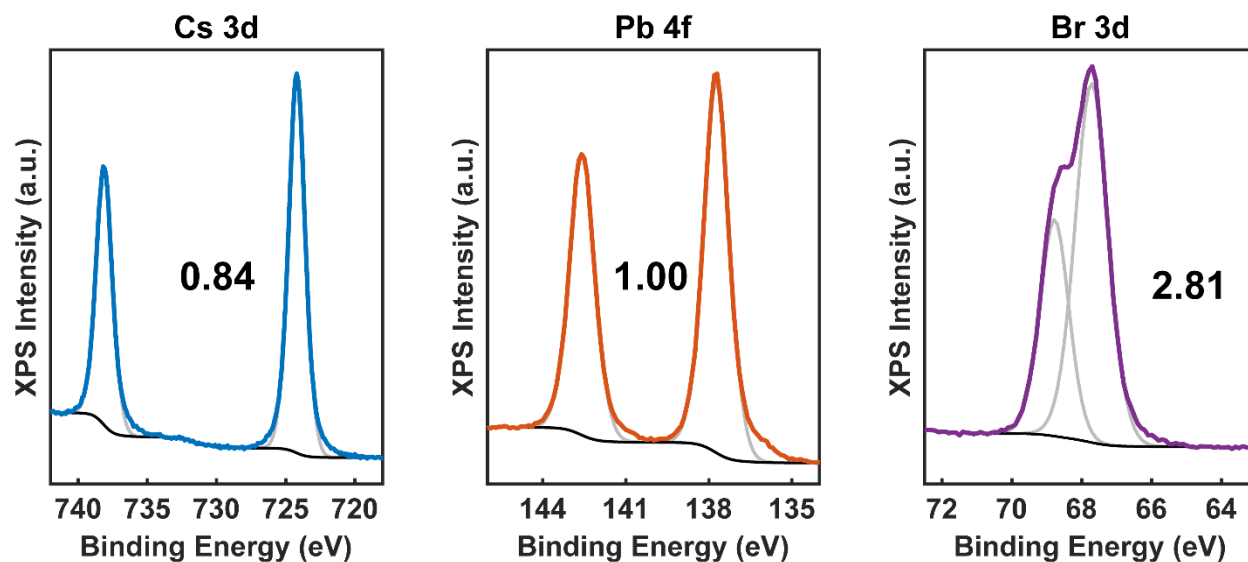


**Figure S2.** X-ray photoelectron spectroscopy results for Sample D, one of the four CsPbBr<sub>3</sub> samples measured, along with fits that yield quantitative integrations for the elemental ratio. Table S1 below contains the results for each of the four samples along with average and standard deviation statistics.

**Table S1.** XPS results for four CsPbBr<sub>3</sub> samples

Sample Name	Cs 3d	Pb 4f	Br 3d
Sample A	0.76	1.00	2.82
Sample B	0.76	1.00	2.86
Sample C	0.77	1.00	2.82
Sample D	0.84	1.00	2.81
<b>Average</b>	<b>0.78±0.04</b>	<b>1.00</b>	<b>2.83±0.02</b>

The signal measured by XPS is an exponentially surface-weighted signal. The expected stoichiometry for a pristine nanocrystal can be predicted from the edge length of the nanocube ( $l$ ), the lattice parameter ( $a$ ), and the inelastic mean free path ( $\lambda$ ). All lengths should be in nanometers. The inelastic mean free path is determined by the X-ray source energy (1486.6 eV in this case) and the binding energies of the elements, as this determines the kinetic energy of the photoelectrons. Kinetic energy can then be converted into inelastic mean free path,  $\lambda$ , with the universal curve (ref).

$$E_{kinetic} = E_{source} - E_{binding}$$

$$\lambda = \frac{143}{E_{kinetic}^2} + 0.054 \cdot \sqrt{E_{kinetic}}$$

The inelastic mean free paths for Pb ( $E_{binding}=140$  eV) and Br ( $E_{binding}=68$  eV) are 1.98 and 2.03 nm, respectively, yielding an average inelastic mean free path for Br/Pb analysis of 2.0 nm. This value describes the attenuation of the photoelectron beam with increasing distance from the surface, and will be used to determine the exponential weighting factor for each layer sampled. First, the atomic composition of each layer, and then the entire nanocrystal, must be determined. Layers are either CsX or PbX<sub>2</sub>, and each will contribute a certain number of atoms based on the number of unit cells present in the nanocrystal. It is useful to consider the edge length of the nanocrystal in terms of unit cells,  $N$ .

$$N = \frac{l}{a} = \frac{9.4 \text{ nm}}{0.587 \text{ nm}} = 16$$

As seen above, these samples are 16 unit cells across on average. The number of Cs, Pb, and X atoms in each layer type (for CsX termination) can now be expressed in terms of  $N$ .

CsX layer (CsX termination):

- Cs =  $(N+1)^2$
- Pb = 0
- X =  $N^2$

PbX<sub>2</sub> layer (CsX termination):

- Cs = 0
- Pb =  $N^2$
- X =  $2N(N+1)$

This allows one to determine the exact atomic composition of these finite crystals (Table S2). Each layer can then be weighted according to its distance from the surface ( $d$ ), together with the inelastic mean free path ( $\lambda$ ). The nanocrystal is terminated by CsX facets.

$$I(d) = I_0 e^{\frac{-d}{\lambda}}$$

**Table S2.** Layer-by-layer composition for a pristine 9.4 nm CsPbX<sub>3</sub> nanocrystal terminated by (001) surfaces and CsX facets (unweighted)

Layer	Distance from Surface (nm)	Exponential Weighting Factor	Total Cs Atoms in Layer	Total Pb Atoms in Layer	Total X Atoms in Layer
CsX	0.000	1.000	289	0	256
PbX <sub>2</sub>	0.294	0.864	0	256	545
CsX	0.587	0.746	289	0	256
PbX <sub>2</sub>	0.881	0.644	0	256	545
CsX	1.174	0.556	289	0	256
PbX <sub>2</sub>	1.468	0.480	0	256	545
CsX	1.761	0.415	289	0	256
PbX <sub>2</sub>	2.055	0.358	0	256	545
CsX	2.348	0.309	289	0	256
PbX <sub>2</sub>	2.642	0.267	0	256	545
CsX	2.935	0.231	289	0	256
PbX <sub>2</sub>	3.229	0.199	0	256	545
CsX	3.522	0.172	289	0	256
PbX <sub>2</sub>	3.816	0.148	0	256	545
CsX	4.109	0.128	289	0	256
PbX <sub>2</sub>	4.403	0.111	0	256	545
CsX	4.696	0.096	289	0	256
PbX <sub>2</sub>	4.990	0.083	0	256	545
CsX	5.283	0.071	289	0	256
PbX <sub>2</sub>	5.577	0.062	0	256	545
CsX	5.870	0.053	289	0	256
PbX <sub>2</sub>	6.164	0.046	0	256	545
CsX	6.457	0.040	289	0	256
PbX <sub>2</sub>	6.751	0.034	0	256	545
CsX	7.044	0.030	289	0	256
PbX <sub>2</sub>	7.338	0.026	0	256	545
CsX	7.631	0.022	289	0	256
PbX <sub>2</sub>	7.925	0.019	0	256	545
CsX	8.218	0.016	289	0	256
PbX <sub>2</sub>	8.512	0.014	0	256	545
CsX	8.805	0.012	289	0	256
PbX <sub>2</sub>	9.099	0.011	0	256	545
CsX	9.392	0.009	289	0	256
<b>TOTAL</b>			<b>4921</b>	<b>4103</b>	<b>13078</b>

A pristine 9.4 nm CsPbX<sub>3</sub> nanocrystal terminated by (001) surfaces and CsX facets possesses an unweighted Cs:Pb:X stoichiometry of 1.2:1:3.2. In light of this, it is important to note if bulk 1:1:3 stoichiometry is measured experimentally, this actually corresponds to a nanocrystal that is deficient in both Cs and X, not a pristine nanocrystal. A stoichiometric correction that accounts for the finite size of the nanocrystal must be considered when analyzing the results of an elemental analysis technique such as XPS or ICP-MS. XPS requires an additional correction for the exponential decay in intensity of the ejected photoelectron beam (Table S3).

**Table S3.** Layer-by-layer composition for a pristine 9.4 nm CsPbX<sub>3</sub> nanocrystal terminated by (001) surfaces and CsX facets (exponentially weighted)

Layer	Distance from Surface (nm)	Exponential Weighting Factor	Total Cs Atoms in Layer	Total Pb Atoms in Layer	Total X Atoms in Layer
CsX	0.000	1.000	289	0	256
PbX <sub>2</sub>	0.294	0.864	0	221	471
CsX	0.587	0.746	216	0	191
PbX <sub>2</sub>	0.881	0.644	0	165	351
CsX	1.174	0.556	161	0	143
PbX <sub>2</sub>	1.468	0.480	0	123	262
CsX	1.761	0.415	120	0	106
PbX <sub>2</sub>	2.055	0.358	0	92	195
CsX	2.348	0.309	89	0	79
PbX <sub>2</sub>	2.642	0.267	0	68	145
CsX	2.935	0.231	67	0	59
PbX <sub>2</sub>	3.229	0.199	0	51	108
CsX	3.522	0.172	50	0	44
PbX <sub>2</sub>	3.816	0.148	0	38	81
CsX	4.109	0.128	37	0	33
PbX <sub>2</sub>	4.403	0.111	0	28	60
CsX	4.696	0.096	28	0	25
PbX <sub>2</sub>	4.990	0.083	0	21	45
CsX	5.283	0.071	21	0	18
PbX <sub>2</sub>	5.577	0.062	0	16	34
CsX	5.870	0.053	15	0	14
PbX <sub>2</sub>	6.164	0.046	0	12	25
CsX	6.457	0.040	11	0	10
PbX <sub>2</sub>	6.751	0.034	0	9	19
CsX	7.044	0.030	9	0	8
PbX <sub>2</sub>	7.338	0.026	0	7	14
CsX	7.631	0.022	6	0	6
PbX <sub>2</sub>	7.925	0.019	0	5	10
CsX	8.218	0.016	5	0	4
PbX <sub>2</sub>	8.512	0.014	0	4	8
CsX	8.805	0.012	4	0	3
PbX <sub>2</sub>	9.099	0.011	0	3	6
CsX	9.392	0.009	3	0	2
<b>TOTAL</b>			<b>1130</b>	<b>863</b>	<b>2834</b>

Consideration of the weighted atomic counts indicates that a pristine 9.4 nm CsPbX<sub>3</sub> nanocrystal is expected to display a Cs:Pb:X stoichiometry of 1.3:1:3.3 when measured by XPS. Thus, the experimentally measured XPS stoichiometry of 0.8:1:2.8 indicates that both Cs and X vacancies are present on the surface. However, as described above, the quantification of these vacancies from XPS is subject to a high degree of error because atoms, particularly halides, can easily be lost when exposed to the ultra-high vacuum and high-energy X-rays. For these reasons, we instead chose to quantify the number of halide vacancies in ambient conditions, which was done using <sup>1</sup>H NMR spectroscopy.

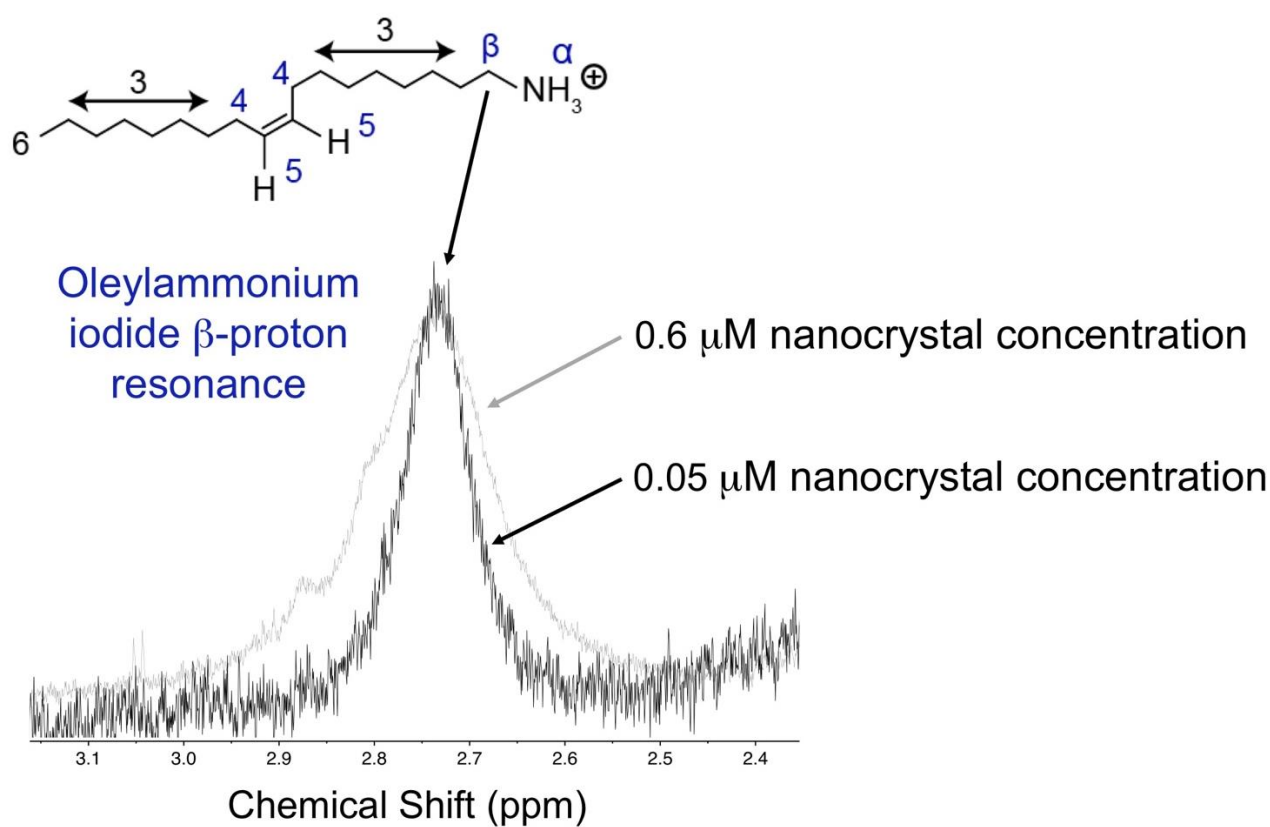


**Figure S3.**  $^1\text{H}$  NMR of the oleylammonium iodide  $\beta$ -protons at the upper and lower bounds of the concentration used for the dilution experiment in Figure 1 of the main text. The peaks are normalized to the same chemical shift and intensity so that their different linewidths can be directly visualized. The linewidth of a ligand in fast exchange is a population-weighted average of free and bound signals,<sup>19</sup> thus a narrowing of the linewidth conclusively demonstrates that the ligand pair equilibrium is shifting away from the surface, thereby introducing new surface halide vacancies.



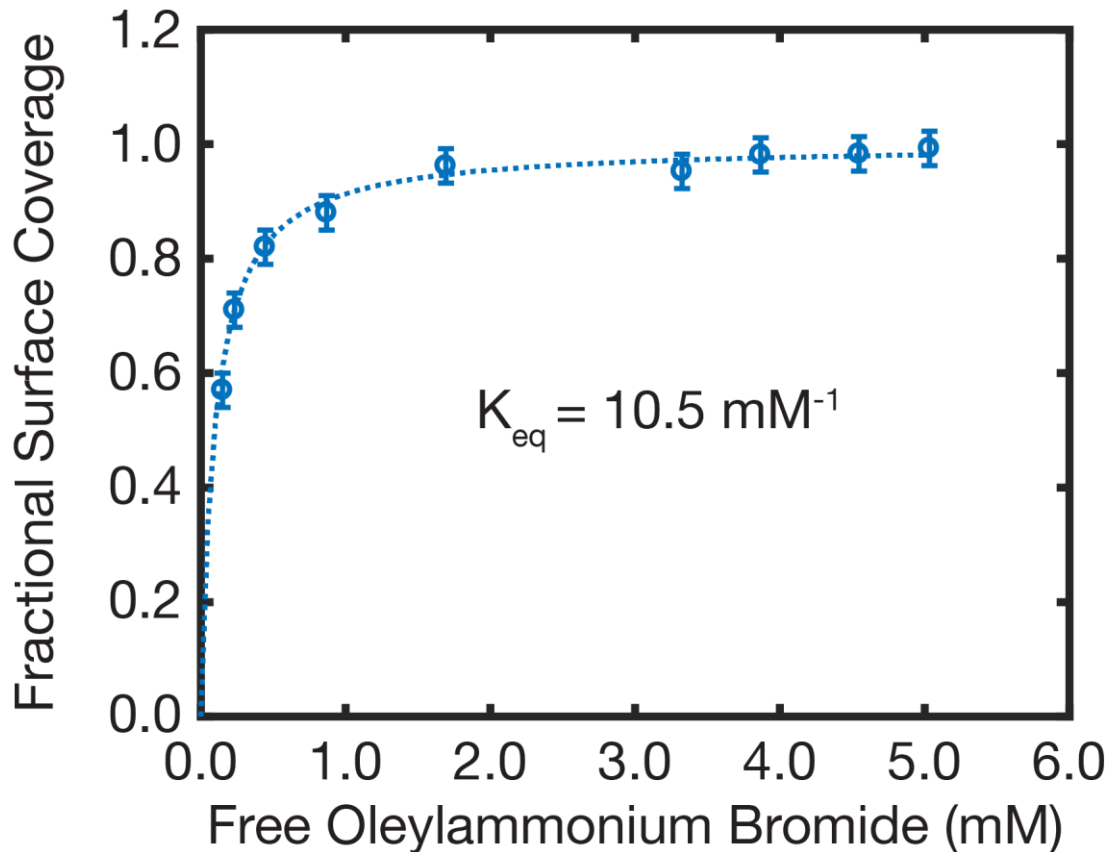


**Figure S4.** Binding isotherm for oleylammonium bromide ligand pairs on the surface of CsPbBr<sub>3</sub> nanocrystals. Data points were generated by analyzing the NMR linewidth of samples with variable ligand pair concentrations. The determination of the bound linewidth of oleylammonium bromide ligands, which is presented later in the SI (Figure S20), allows one to convert the measured linewidth into free and bound fractions, which can then be converted to a fractional surface coverage. The free oleylammonium bromide concentration was determined using the model that was used to fit the PLQY vs. nanocrystal concentration in Figure 1 of the main text (page S8).

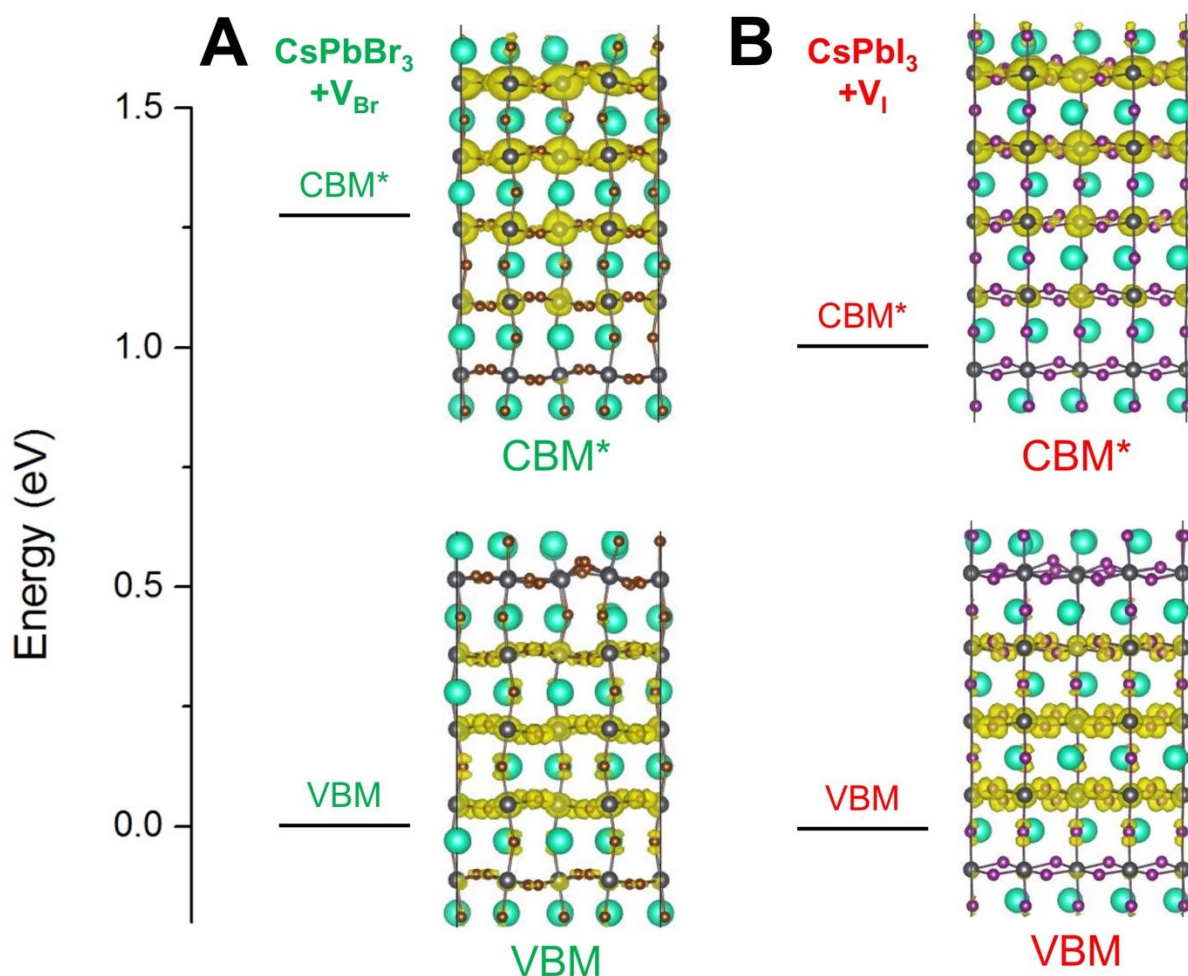


**Figure S5.** Electronic structure calculations and charge density plots at the GGA–PBE+SOC level of theory for (A)  $\text{CsPbBr}_3$  with a surface Br vacancy ( $\text{CsPbBr}_3 + \text{V}_{\text{Br}}$ ), and (B)  $\text{CsPbI}_3$  with a surface I vacancy ( $\text{CsPbI}_3 + \text{V}_{\text{I}}$ ). Both systems appear nominally trap-free. However, the generalized gradient approximation of GGA–PBE is well-known to dramatically underestimate the bandgap, which in this case prohibits the observation of the full set of energy levels presented in the main text. A closer look at the higher energy state, which could be assigned as the CBM, shows a weak localization towards the halide-deficient surface. This stands in contrast to the fully delocalized nature of a typical CBM state. Comparison against the HSE+SOC calculations from the main text, which produce accurate bandgap values, reveals that these higher energy states are actually the shallow defect levels, not the CBM, thus we denote them CBM\* here. This highlights the importance of using a high level of theory when examining shallow defect levels in these systems.

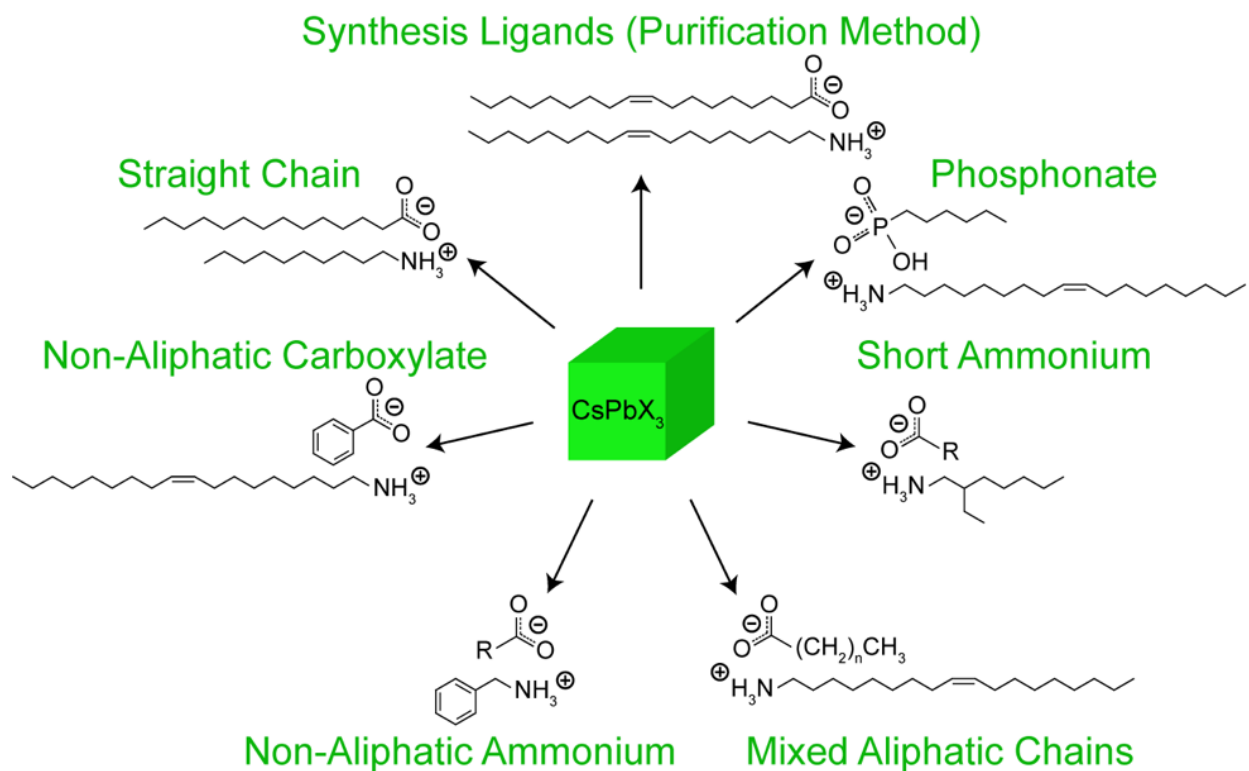


**Figure S6.** Schematic representation of the various ligand exchanges that can be performed using the method introduced in the main text.

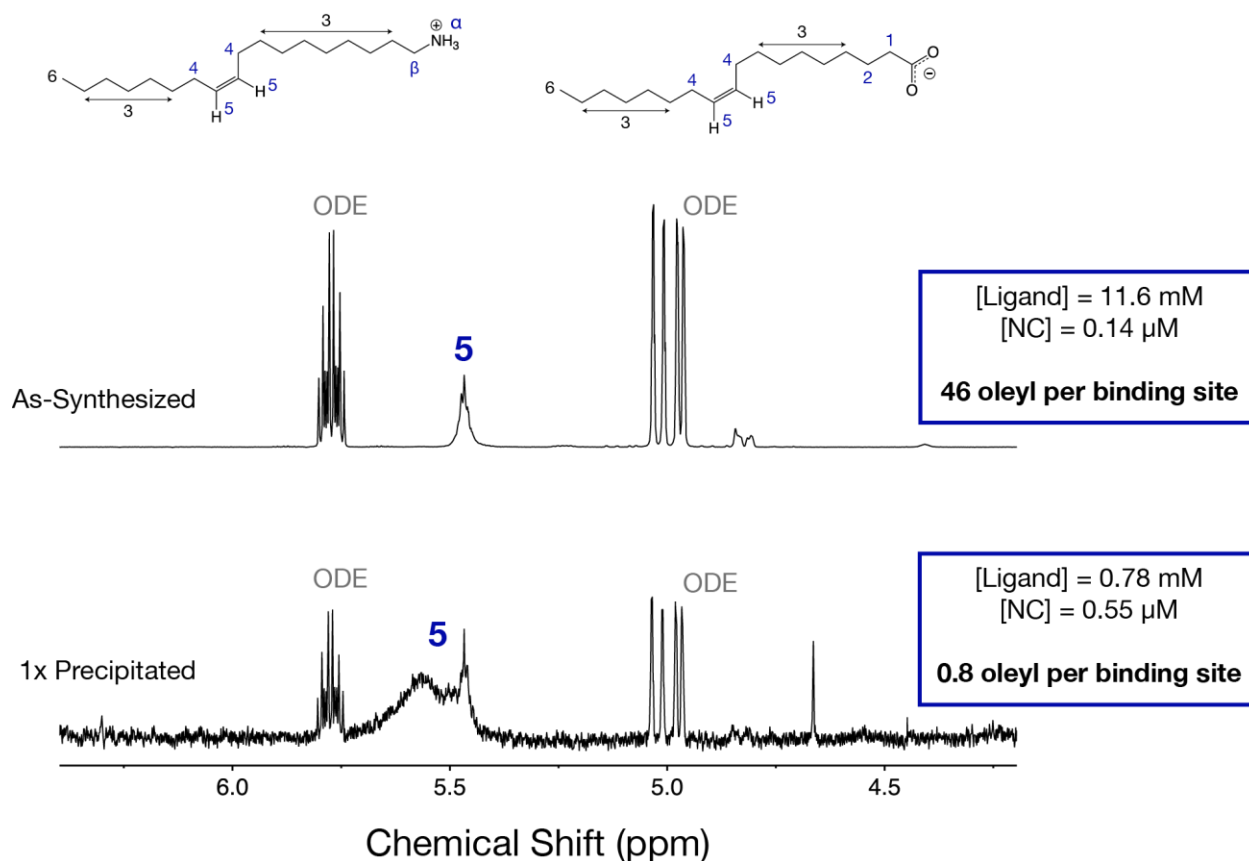


**Figure S7.**  $^1\text{H}$  NMR spectra of an as-synthesized nanocrystal sample and a nanocrystal sample that was precipitated once and then resuspended in neat solvent. Quantitative  $^1\text{H}$  NMR was used to investigate the surface ligand coverage before and after a precipitation and resuspension step. Samples were resuspended in deuterated toluene, and a known amount of an inert internal standard (mesitylene) was added to each sample. Following precise determination of the  $90^\circ$  radio frequency pulse, NMR spectra were collected with a pre-scan delay time of 60 s to ensure complete relaxation of the  $^1\text{H}$  nuclei, which is essential for accurate quantitative measurements. As mentioned in the main text, nanocrystal samples that are isolated following a synthesis have a large excess of ligand, along with ODE and other unknown impurities. However, we found that the majority of this excess ligand is removed upon precipitation and resuspension. The resulting nanocrystal sample was found to have slightly less than 1 ligand per available binding site, and the suspension is no longer bright green. The ligand exchange method introduced in the main text directly exploits the ease with which surface ligands can be removed with this process.

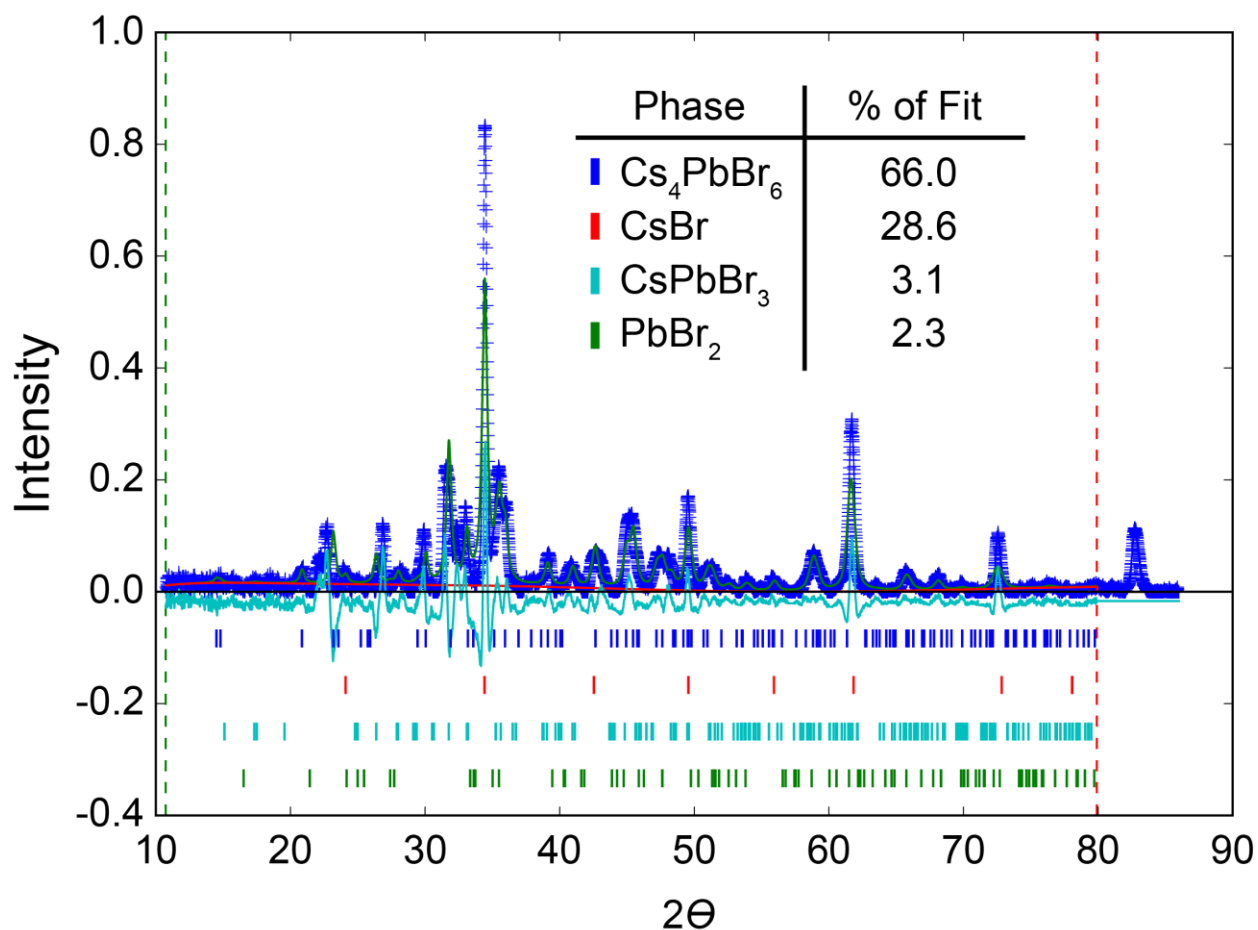


**Figure S8.** X-ray diffraction pattern of the off-white precipitate that forms when a ligand exchange is conducted on  $\text{CsPbBr}_3$  nanocrystals using only amine or acid, but not both species. Only a small fraction ( $\sim 3\%$ ) of nanocrystals are retained in the desired  $\text{CsPbBr}_3$  phase, while the majority degrade into  $\text{CsBr}$  and  $\text{Cs}_4\text{PbBr}_6$  phases. The contribution of each phase to the overall refinement is presented in the table.

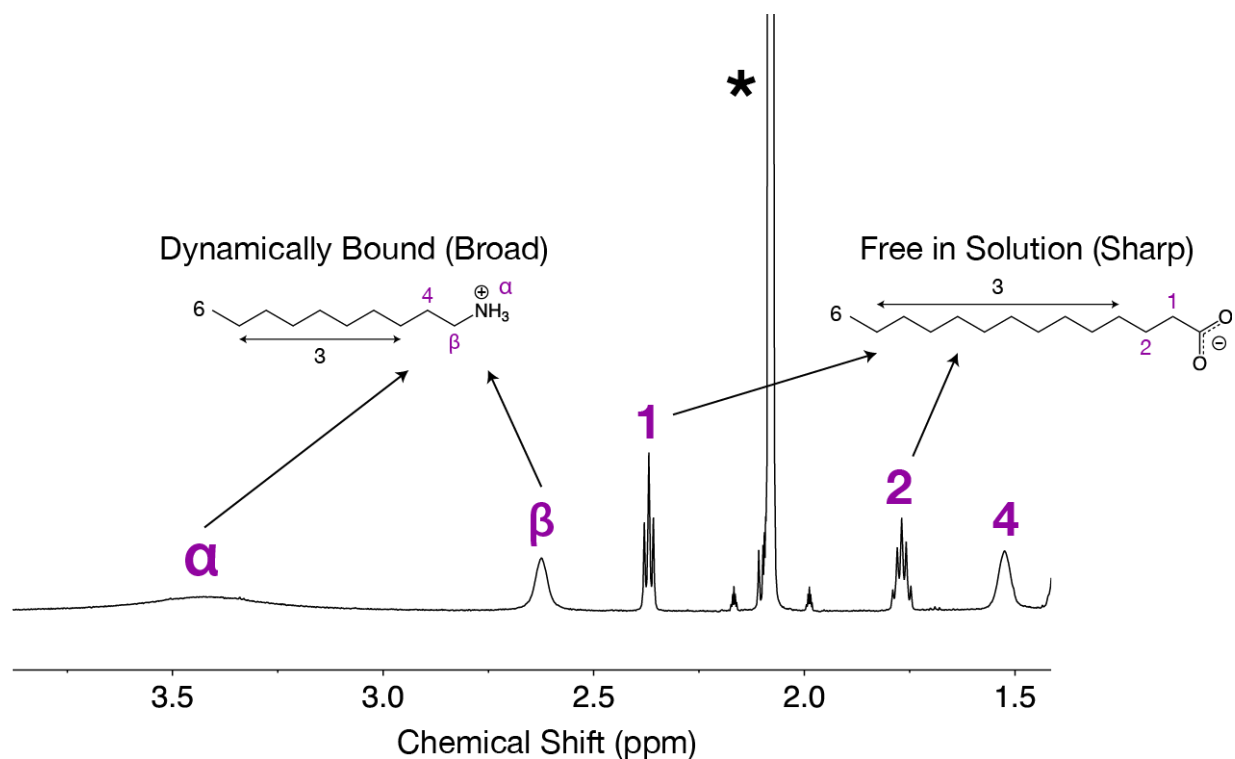


**Figure S9.** A closer look at the alkyl region of the  $^1\text{H}$  NMR spectrum measured for a  $\text{CsPbBr}_3$  nanocrystal sample 3x exchanged to decylammonium and myristate, Figure 4 of the main text. Sharp peaks with the expected fine structure (a triplet and a quintet) are clearly observed for resonances **1** and **2** of myristate, characteristic of molecules rotating freely in solution. In contrast, resonances  $\alpha$ ,  $\beta$ , and **4** of decylammonium feature broad peaks without the expected fine structure, characteristic of molecules interacting with a nanocrystal surface. The broadening of resonances **4** and  $\beta$  are particularly illustrative given that the  $\alpha$  resonance is also broadened by proton exchange. This reinforces observations from ourselves and others about long-chain, harder carboxylates like myristate and oleate tending to be absent from the ligand shell.

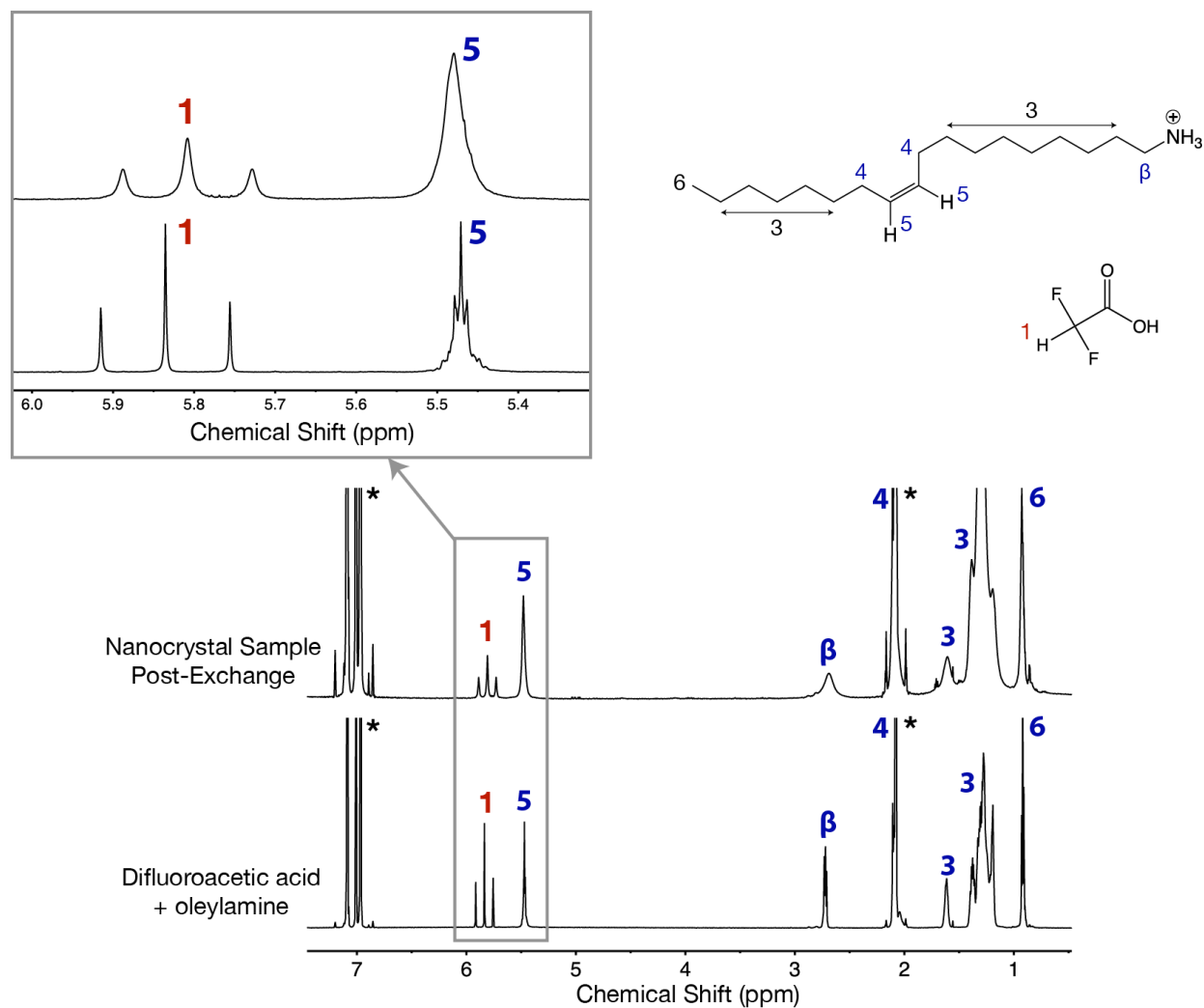


**Figure S10.**  $^1\text{H}$  NMR spectrum of  $\text{CsPbBr}_3$  nanocrystals 3x exchanged to difluoroacetate-oleylammonium ligand pairs, with a reference spectrum of the same ligand pair free in solution included below the nanocrystal sample. In the presence of nanocrystals, each species of the ligand pair displays broadened resonances, which are characteristic of interaction with the surface.

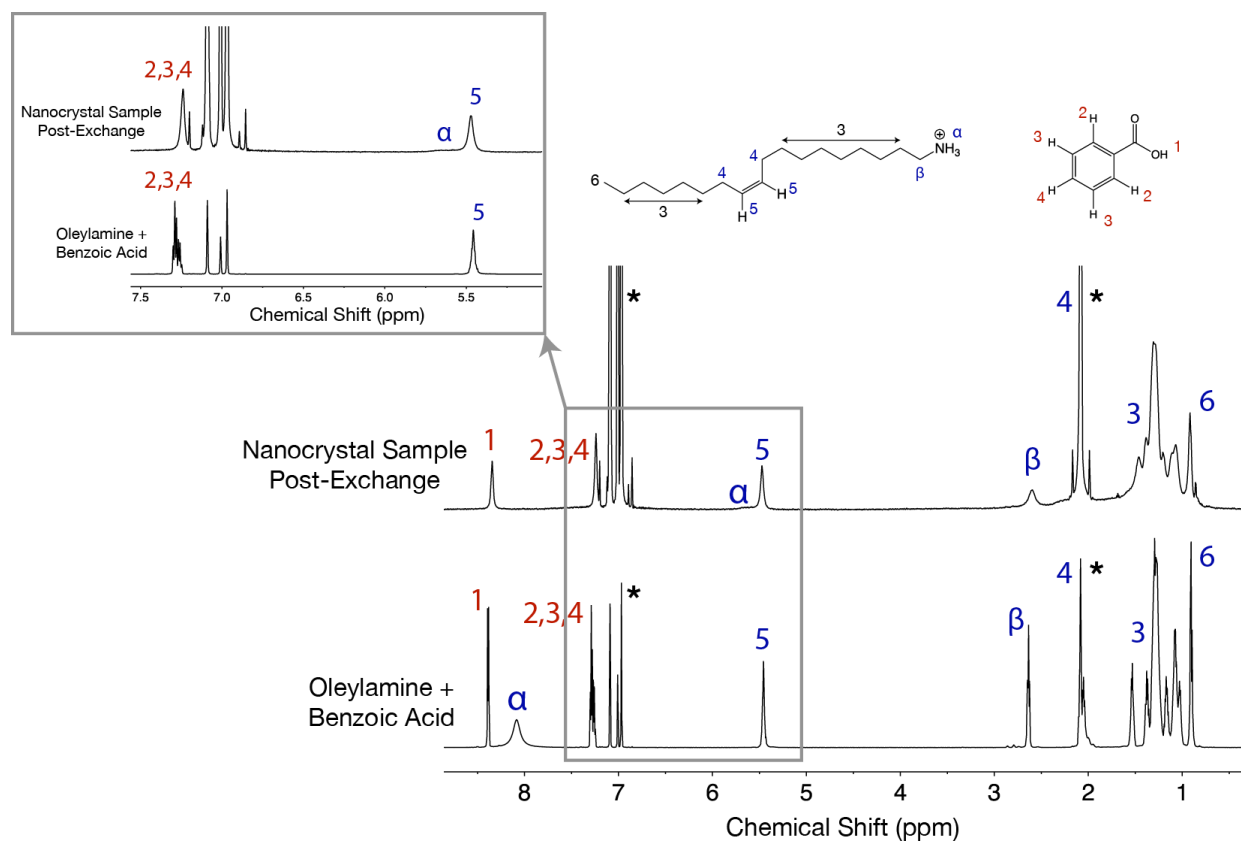


**Figure S11.**  $^1\text{H}$  NMR spectrum of CsPbBr<sub>3</sub> nanocrystals 3x exchanged to benzoate-oleylammonium ligand pairs, with a reference spectrum of the same ligand pair free in solution included below the nanocrystal sample. In the presence of nanocrystals, each species of the ligand pair displays broadened resonances, which are characteristic of interaction with the surface.



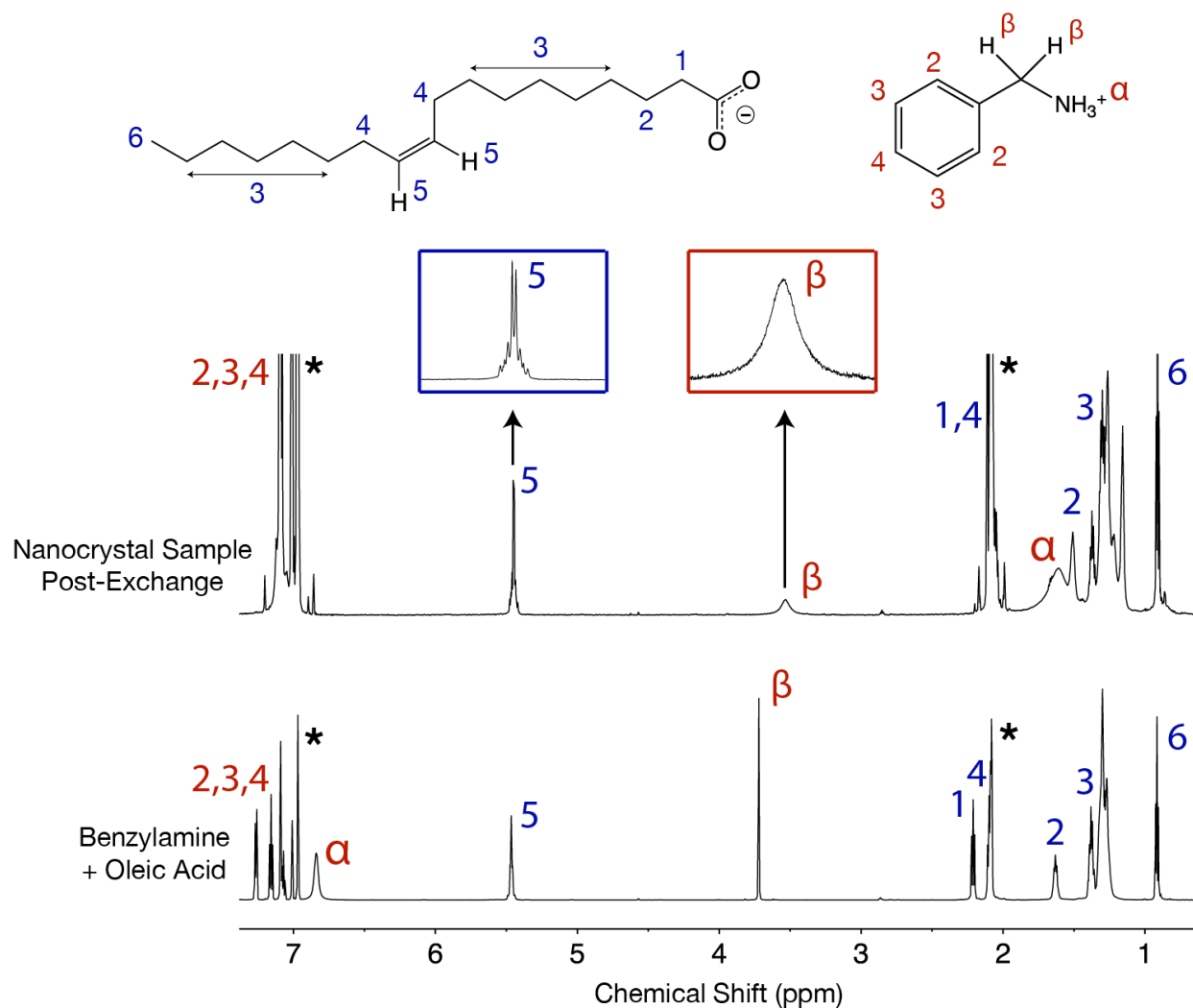


**Figure S12.**  $^1\text{H}$  NMR spectrum of  $\text{CsPbBr}_3$  nanocrystals 3x exchanged to benzylammonium-oleate ligand pairs, with a reference spectrum of the same ligand pair free in solution included below the nanocrystal sample. Resonance 5 from oleate shows no broadening, further supporting existing literature regarding the absence of oleate in the ligand shell. In contrast, the  $\beta$  resonance of benzylammonium broadens significantly when nanocrystals are present, indicating this molecule is acting as a capping ligand.

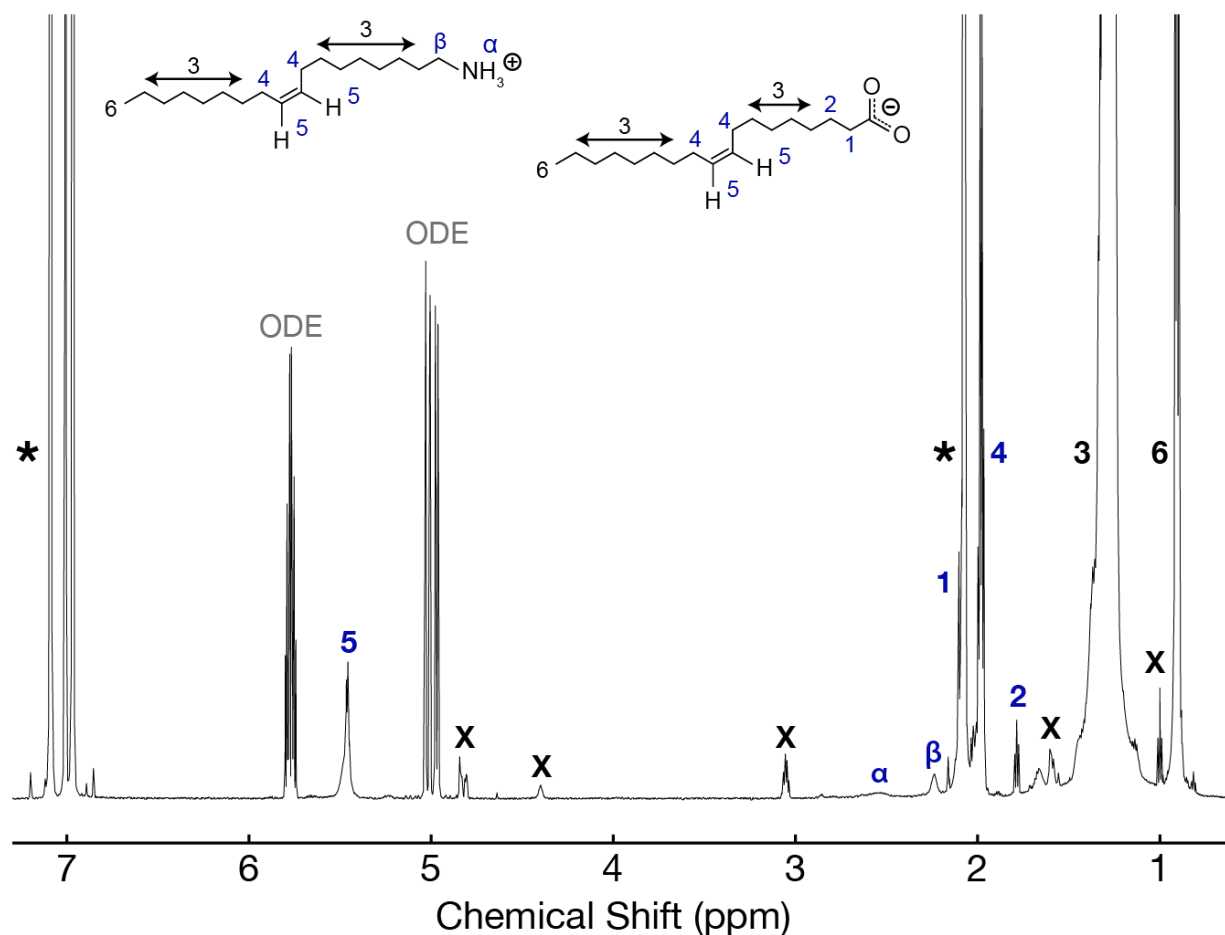


**Figure S13.**  $^1\text{H}$  NMR spectrum of as-synthesized  $\text{CsPbBr}_3$  nanocrystals isolated according to standard literature methods. Residual solvent (ODE) and several unknown impurities (X) are present, along with a complex mixture of oleylammonium bromide, lead oleate, oleylamine, and oleic acid (5). This highlights the need for a purification method such as the one introduced in the main text. Three of the five impurities can be identified as originating from impure precursors (ODE, oleylamine, and oleic acid). The remaining impurities do not originate from a precursor, and thus are ascribed as post-synthetic impurities. The resonance around 3.06 ppm was also observed by De Roo et. al.,<sup>20</sup> and is presumably the amide of oleic acid and oleylamine.

**Table S4.** Assignment of impurities present in as-synthesized, isolated  $\text{CsPbBr}_3$  nanocrystals

Impurity	Chemical Shift (ppm)	Assignment
	4.83	Impurity present in ODE
	4.40	Unknown (post-synthetic)
	3.06	Amide (post-synthetic)
	1.60	Impurity present in oleylamine
	1.01	Impurity present in ODE

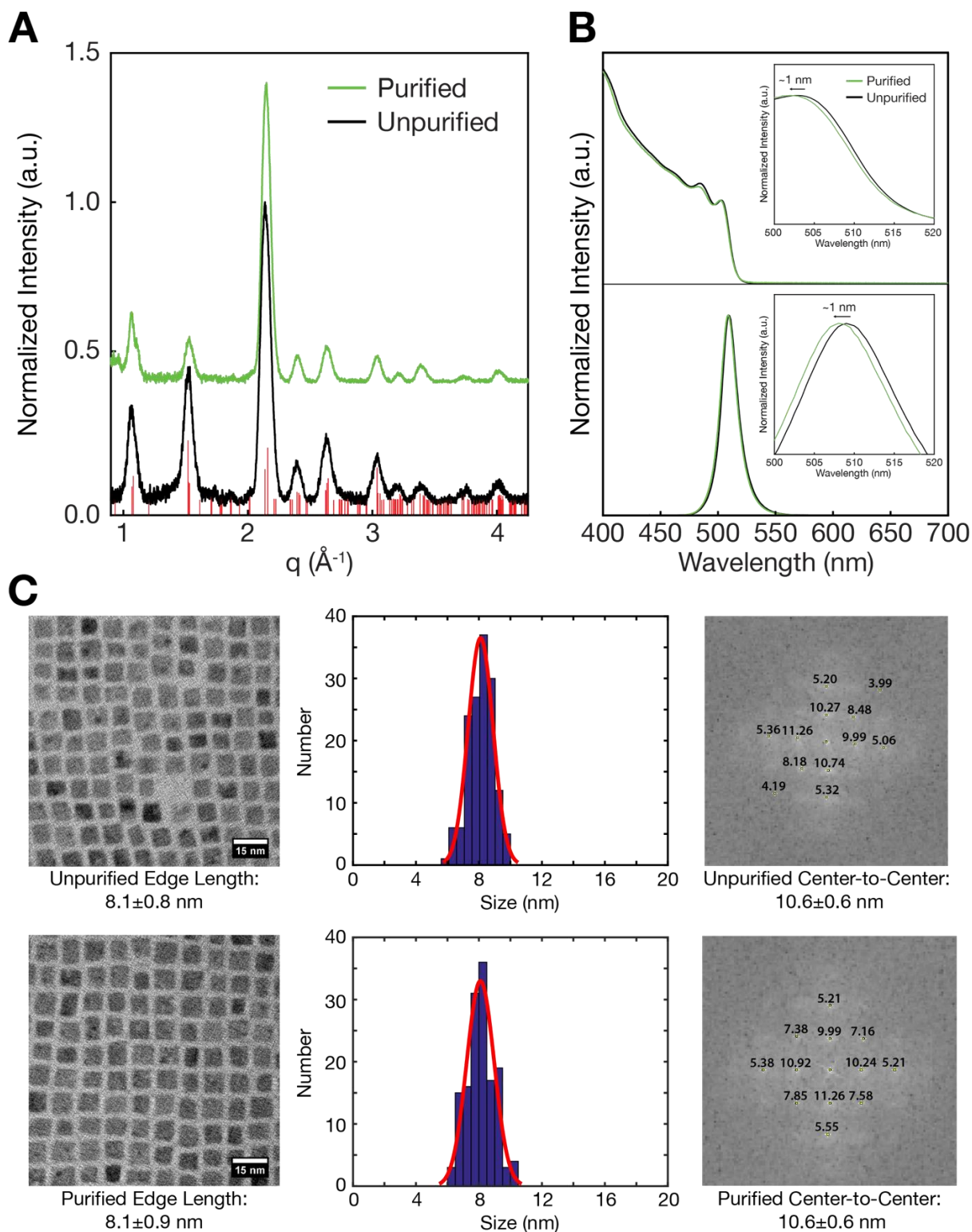


**Figure S14.** (A) X-ray diffraction patterns, (B) absorbance and fluorescence spectra, and (C) TEM images (left) with size distributions (middle) and interparticle spacing (right) of  $\text{CsPbBr}_3$  nanocrystals before and after purification. Purification leaves nanocrystal size, shape, and ligand coverage virtually unchanged. For each image, 75 particles were measured for the histogram.

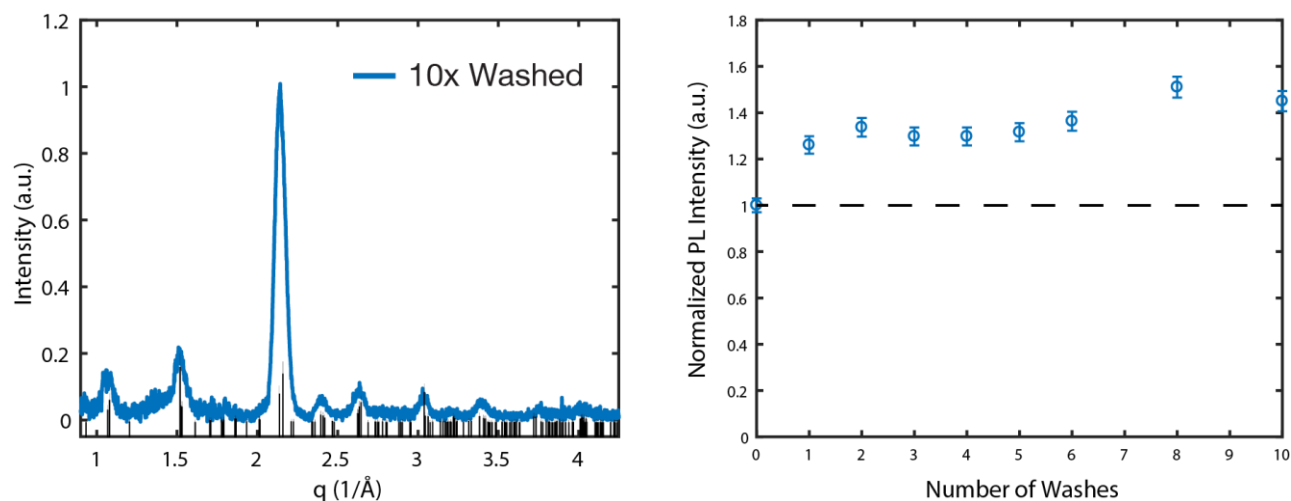


**Figure S15.** Demonstration of the benign nature of the purification process. XRD pattern of a sample washed 10 $\times$  instead of the standard 3 $\times$ , and PL intensity measured along each step of the same process. XRD shows the orthorhombic perovskite phase with no  $\text{Cs}_4\text{PbBr}_6$  peaks present, indicating that the entire sample is preserved in the desired  $\text{CsPbBr}_3$  phase. The PL intensity also behaves as expected. All samples were measured at identical nanocrystal concentration, thus PL intensity is a direct reflection of PLQY. The initial removal of lead oleate increases PLQY (Figure S25). After lead oleate is removed, PLQY is unchanged within measurement error for several more washes, and then it starts to increase again for 8 and 10 washes. We attribute this final increase to the gradual loss of nanocrystals – resuspending slightly fewer nanocrystals in the same concentration of ligand throughout yields a slightly higher ligand:nanocrystal ratio, thus shifting the dynamic ligand equilibrium towards the surface.

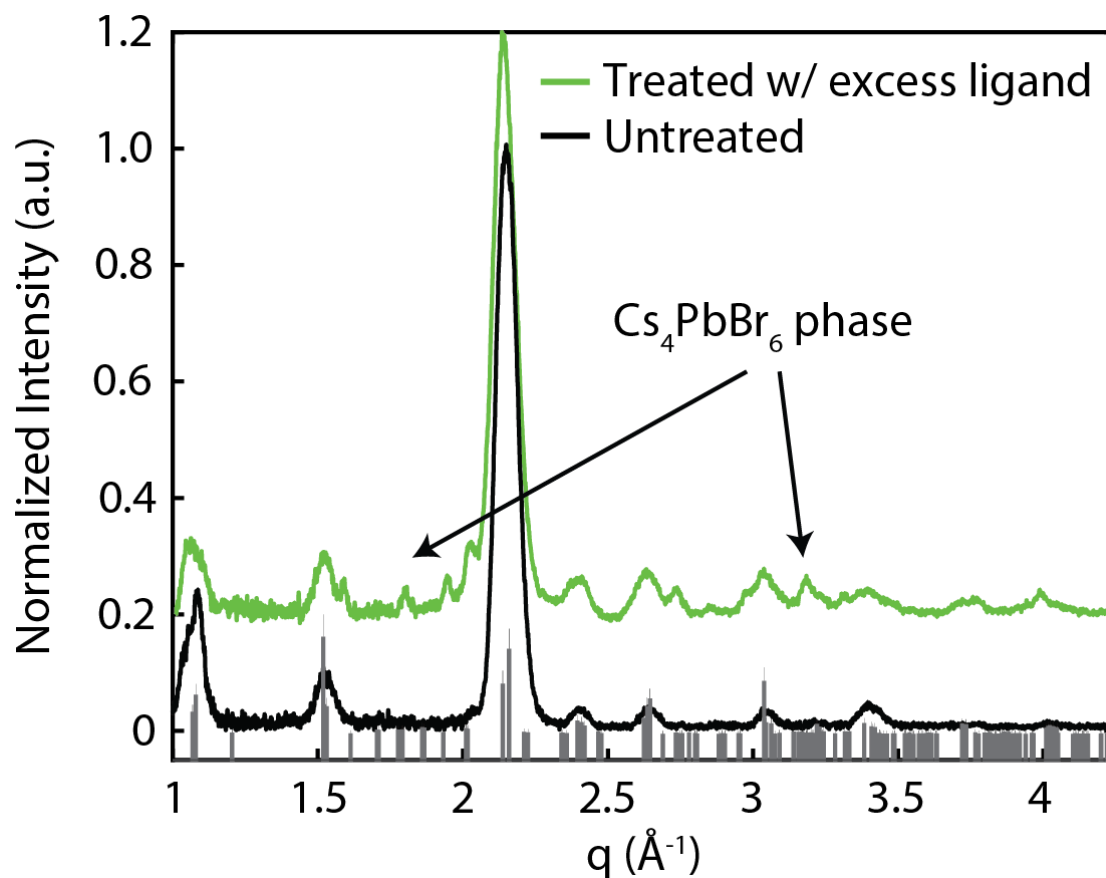


**Figure S16.** XRD pattern of an untreated sample (black) and a sample 3x treated (green) with an excess of oleylammonium-oleate pairs. Approximately 30 ion pairs per available nanocrystal binding site were used. Care must be taken to preserve the entire sample in the desired CsPbBr<sub>3</sub> phase. Treatment with an excess of ligand yields partial transformation to the Cs<sub>4</sub>PbBr<sub>6</sub> phase, which is not surprising given the growing body of literature about ligand-mediated transformations between CsPbBr<sub>3</sub> and Cs<sub>4</sub>PbBr<sub>6</sub> nanocrystals.<sup>21-23</sup>

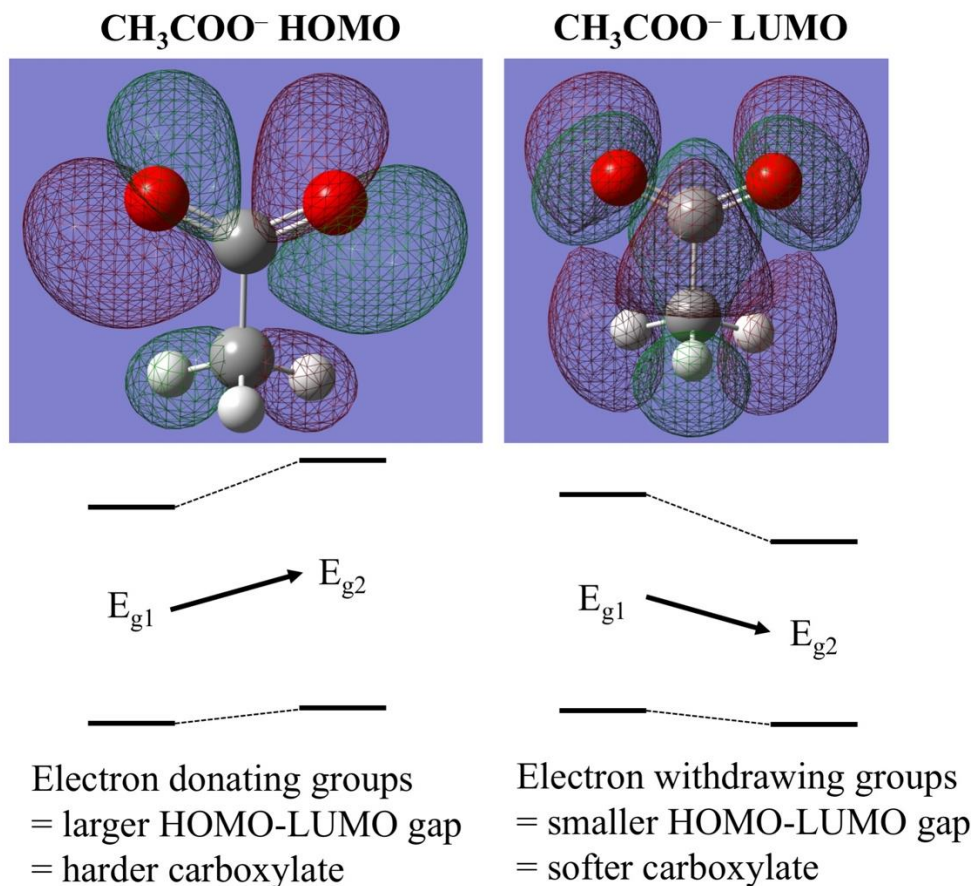


**Figure S17.** Density functional theory (DFT) calculations of the acetate anion. The HOMO is localized primarily on the O atoms of COO<sup>-</sup>, while the LUMO is primarily on the C atom of COO<sup>-</sup>. Because C is less electronegative than O, the LUMO energy will be changed more significantly by electron donating/withdrawing groups than will the HOMO. Electron donating groups are expected to increase the HOMO-LUMO gap by destabilizing the LUMO more than the HOMO, whereas electron withdrawing groups are expected to decrease the HOMO-LUMO gap by stabilizing the LUMO more than the HOMO. Smaller HOMO-LUMO gaps correspond to softer, more polarizable binding heads, thus we investigated new carboxylate with electron withdrawing tail groups, namely fluoroacetate, difluoroacetate, trifluoroacetate, and benzoate. DFT calculations confirm that these species have smaller HOMO-LUMO gaps than acetate, and thus are softer, as shown in Table S5. In contrast, an electron donating alkyl chain (e.g. for pentanoate) yields a larger HOMO-LUMO gap, and thus a harder carboxylate.

**Table S5.** HOMO-LUMO gap energies for various carboxylate anions

Anion	HOMO-LUMO gap (eV)
Acetate	11.07
Fluoroacetate	11.02
Difluoroacetate	10.78
Trifluoroacetate	10.47
Benzoate	7.40
Pentanoate	11.35

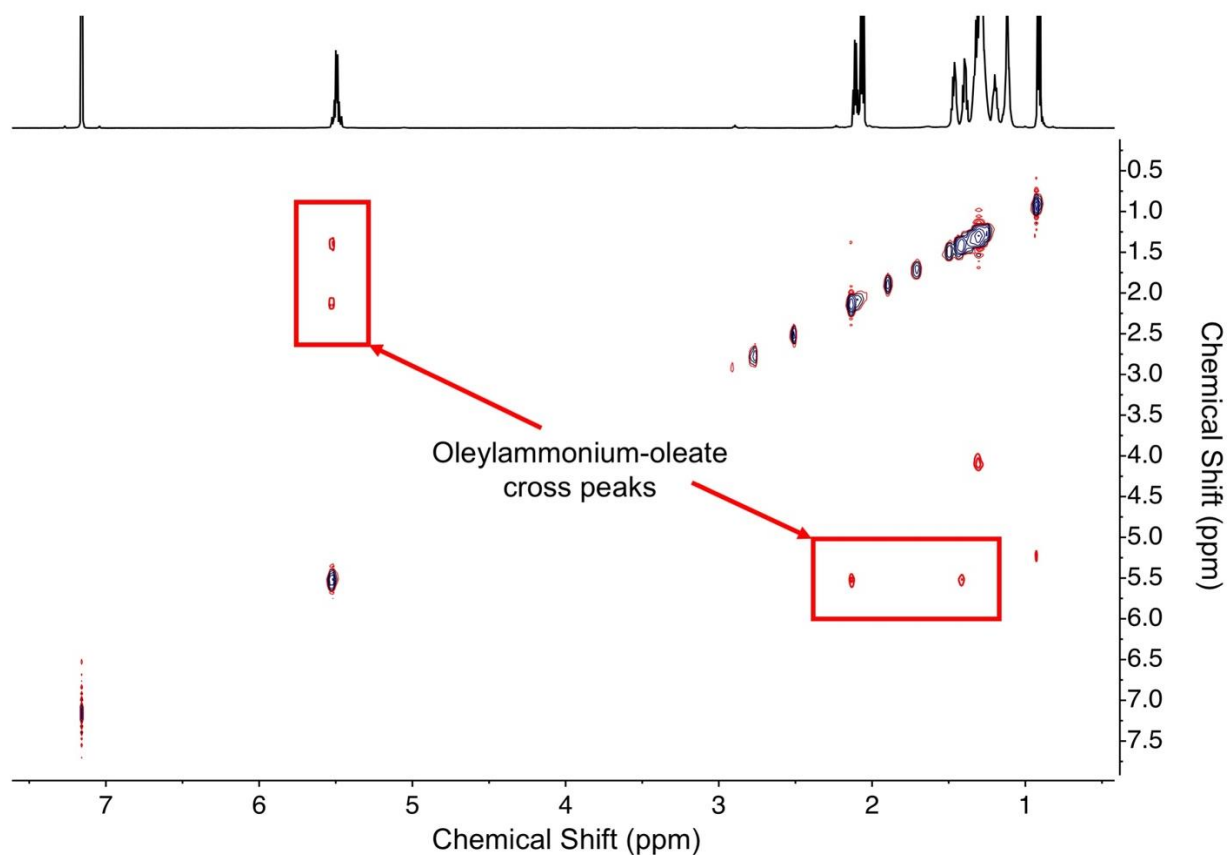


**Figure S18.** Example  $^1\text{H}$  NOESY NMR spectrum of ligands pairs free in solution without the presence of nanocrystals. In this case, the ligand pair is oleylammonium-oleate. These species display positive (red) NOE signals, which is characteristic of the rapid tumbling of small molecules. This stands in contrast to the negative (black) NOE signals presented for the ligand pairs plus nanocrystals in the main text. This change in sign indicates that the tumbling frequency of ligand pairs decreases significantly in the presence of nanocrystals, thereby confirming their interaction with the nanocrystal surface.

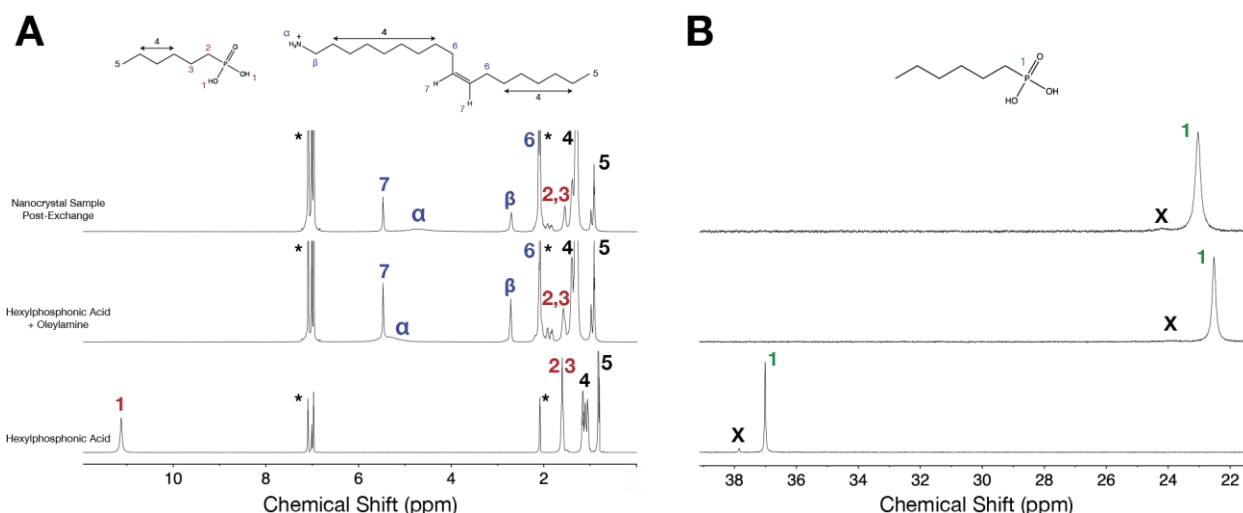


**Figure S19.** A) <sup>1</sup>H and B) <sup>31</sup>P NMR spectra of CsPbBr<sub>3</sub> nanocrystals 3x exchanged to oleylammonium-hexylphosphonate ligand pairs, with reference spectra of the same ligand pair free in solution included below the nanocrystal sample, along with reference spectra of hexylphosphonic acid alone. The <sup>31</sup>P provide strong evidence that hexylphosphonate is interacting with the nanocrystal surface, which we confirm with NOESY in the main text. As ion pairs are formed, hexylphosphonic acid is deprotonated, thus more electron density resides on the P atom of interest (green resonance 1). This is confirmed by the upfield shift in B). Additionally, some peak broadening occurs due to proton exchange, which is also consistent with ion pair formation. When the ion pair solution is used for a nanocrystal ligand exchange, the P resonance broadens considerably, consistent with binding to the nanocrystal surface. Finally, the phosphonate is expected to bind to surface Pb, which should shift some electron density off of the P atom due to the positive charge of Pb. <sup>31</sup>P NMR corroborates this, as the nanocrystal peak is shifted downfield from the ion pair peak, indicating less electron density is present on the P atom when these molecules are acting as nanocrystal capping ligands.



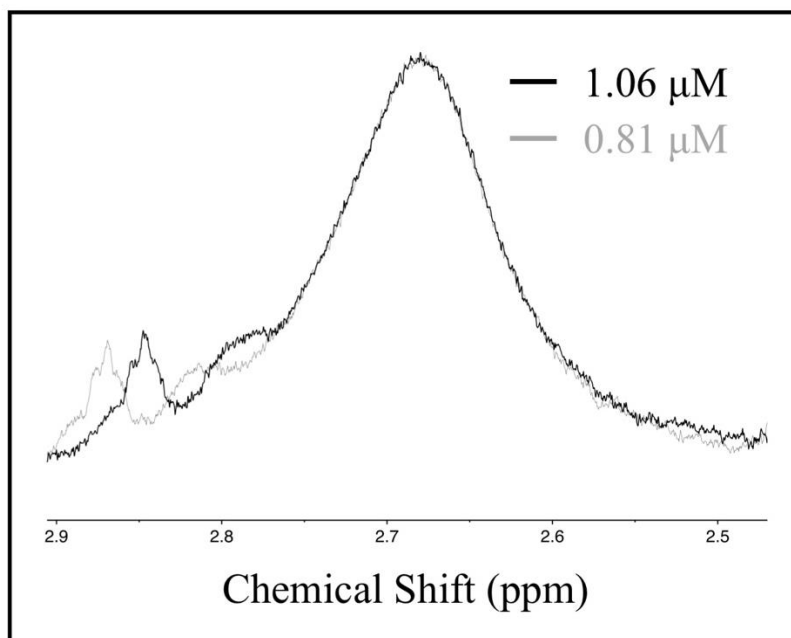


**Figure S20.**  $^1\text{H}$  NMR of two different high concentrations of  $\text{CsPbBr}_3$  nanocrystals and their native ligands, namely the oleylammonium bromide  $\beta$ -protons. The peaks are normalized to the same chemical shift and intensity so that their linewidths can be directly compared. The linewidth of a ligand in fast exchange is a population-weighted average of free and bound signals,<sup>19</sup> thus no measurable change in the NMR linewidth demonstrates that the ligand equilibrium remains unchanged in this high concentration region.

The demonstration of an essentially unchanged free vs. bound ligand equilibrium indicates that the nanocrystal surface is saturated at these high concentrations. This allows one to assume that all available binding sites on the nanocrystal surface are occupied. Knowledge of the nanocrystal morphology and lattice constant allow the number of binding sites to be calculated, which then enables the determination of the linewidth of bound ligands in this system. As stated above, the linewidth of a ligand in fast exchange is a weighted average of free and bound populations, which is expressed below.

$$\lambda_{obs} = P_{free}\lambda_{free} + P_{bound}\lambda_{bound}$$

$\lambda$  is the linewidth and  $P$  is the relative population.

$$\lambda_{bound} = \frac{\lambda_{obs} - P_{free}\lambda_{free}}{P_{bound}}$$

$$P_{bound} = \frac{N_{bound}}{N_{total}}$$

The demonstration of a saturated surface allows the number of ligands per nanocrystal,  $N_{\text{bound}}$ , which is currently unknown, to be replaced with the number of binding sites per nanocrystal,  $N_{\text{sites}}$ , which can readily be calculated from the nanocrystal morphology and the maximum theoretical ligand density of  $2.9/\text{nm}^2$ .  $N_{\text{total}}$  can be determined by quantitative  $^1\text{H}$  NMR, referenced to an internal standard.

$$P_{\text{bound}} = \frac{N_{\text{sites}}}{N_{\text{total}}}$$

$$\lambda_{\text{bound}} = \frac{\lambda_{\text{obs}} - \left(1 - \frac{N_{\text{sites}}}{N_{\text{total}}}\right) \lambda_{\text{free}}}{\frac{N_{\text{sites}}}{N_{\text{total}}}}$$

For this particular nanocrystal sample, we determined  $\lambda_{\text{bound}} = \mathbf{288\text{ Hz}}$ . This is consistent with slow tumbling of ligands as they interact with a relatively large nanocrystal. It should be noted that this linewidth is specifically for proton resonances that are directly adjacent to the binding head. Conveniently, difluoroacetate also has a spectrally isolated proton resonance that is directly adjacent to the binding head, and thus this bound linewidth can also be used with nanocrystal samples following a ligand exchange to oleylammonium-difluoroacetate pairs. These protons can be directly compared to the oleylammonium  $\beta$ -protons since they are equidistant from the nanocrystal surface, they display comparable linewidths when measured free in solution, and they are not broadened by proton exchange, therefore broadening beyond a free linewidth can be attributed entirely to surface binding. Together, this allows the number of new Pb-difluoroacetate bonds to be directly quantified.

$$\lambda_{\text{obs}} = P_{\text{free}}\lambda_{\text{free}} + P_{\text{bound}}\lambda_{\text{bound}}$$

$$P_{\text{bound}} = \frac{\lambda_{\text{obs}} - P_{\text{free}}\lambda_{\text{free}}}{\lambda_{\text{bound}}}$$

$$N_{\text{bound}} = N_{\text{total}} \left( \frac{\lambda_{\text{obs}} - \lambda_{\text{free}}}{\lambda_{\text{bound}} - \lambda_{\text{free}}} \right)$$

$N$  now refers to the number of difluoroacetate ligands rather than oleylammonium ligands. As described in the main text, a high concentration of  $\text{CsPbBr}_3$  nanocrystals following a ligand exchange to oleylammonium-difluoroacetate pairs displayed a linewidth ( $\lambda_{\text{obs}}$ ) of  $10.7 \pm 0.2\text{ Hz}$ , and with knowledge of free and bound linewidths along with  $N_{\text{total}}$ ,  $N_{\text{bound}}$  is determined to be  $180 \pm 20$ . This result is in close agreement with the determination of  $190 \pm 20$  halide vacancies for 60-65% PLQY  $\text{CsPbBr}_3$  samples from the simple trapping model used to fit the data in Figure 1.

Knowledge of  $\lambda_{\text{bound}}$  also allowed the free vs. bound equilibrium constant,  $K_{\text{eq}}$ , to be determined for oleylammonium bromide (Figure S4).

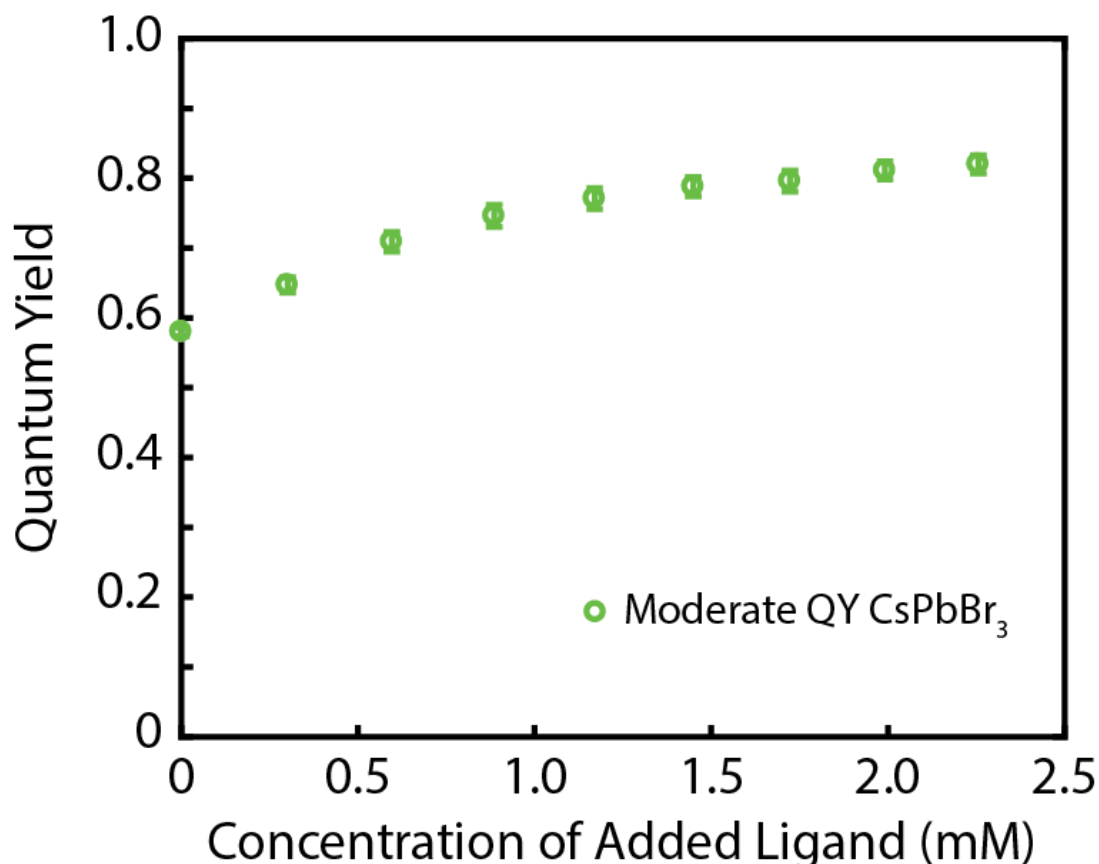


**Figure S21.** PLQY of CsPbBr<sub>3</sub> nanocrystals as a function of additional native ligand (oleylammonium-oleate) concentration, measured with an integrating sphere spectrofluorometer. Nanocrystal concentration was held constant as a solution of oleylammonium-oleate ion pairs was gradually added, with PLQY being remeasured after each addition. This result can be readily understood with the dynamic ligand shell. Increasing the amount of free ligand in solution shifts the overall equilibrium towards bound ligands, thus PLQY increases. Figure 1 of the main text demonstrated a similar effect, but with nanocrystal concentration rather than ligand concentration. Taken together, we show that the same CsPbBr<sub>3</sub> nanocrystal sample can have a measured PLQY ranging all the way from  $0.52 \pm 0.03$  to  $0.83 \pm 0.03$  based on variations in nanocrystal and ligand concentration. If one is going to draw a conclusion about certain ligands being more effective than others for surface passivation based on optical measurements, such as in the main text, a meaningful comparison is one where samples have identical concentrations of nanocrystals and ligands, and they must also be measured at identical concentrations.

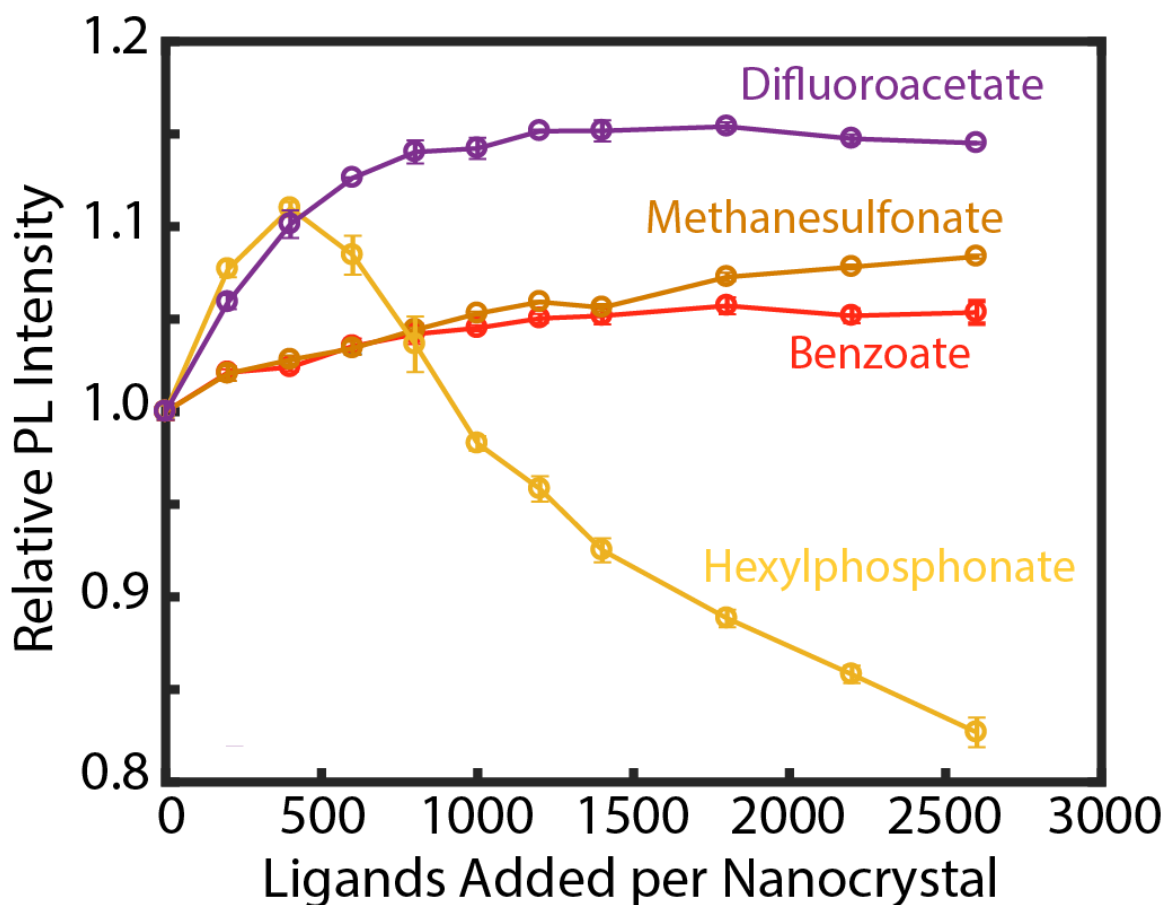


**Figure S22.** Comparison of the effect of various softer binding heads on CsPbBr<sub>3</sub> nanocrystal PL intensity. All ligand solutions were prepared with oleylammonium as a counterion. Ligand solutions were slowly titrated into cuvettes of dilute CsPbBr<sub>3</sub> nanocrystals, and PL was measured several times after each addition to ensure an equilibrium value. These results suggest that hexylphosphonate and difluoroacetate are the most effective for binding under-coordinated Pb atoms. In fact, Pb-phosphonate bond strengths can exceed those of the crystal cohesive energy, resulting in degradation of the nanocrystal when too much phosphonate is added, as observed here. However, so long as care is taken, near-unity PLQY CsPbBr<sub>3</sub> nanocrystals can be achieved, as was demonstrated in the main text.

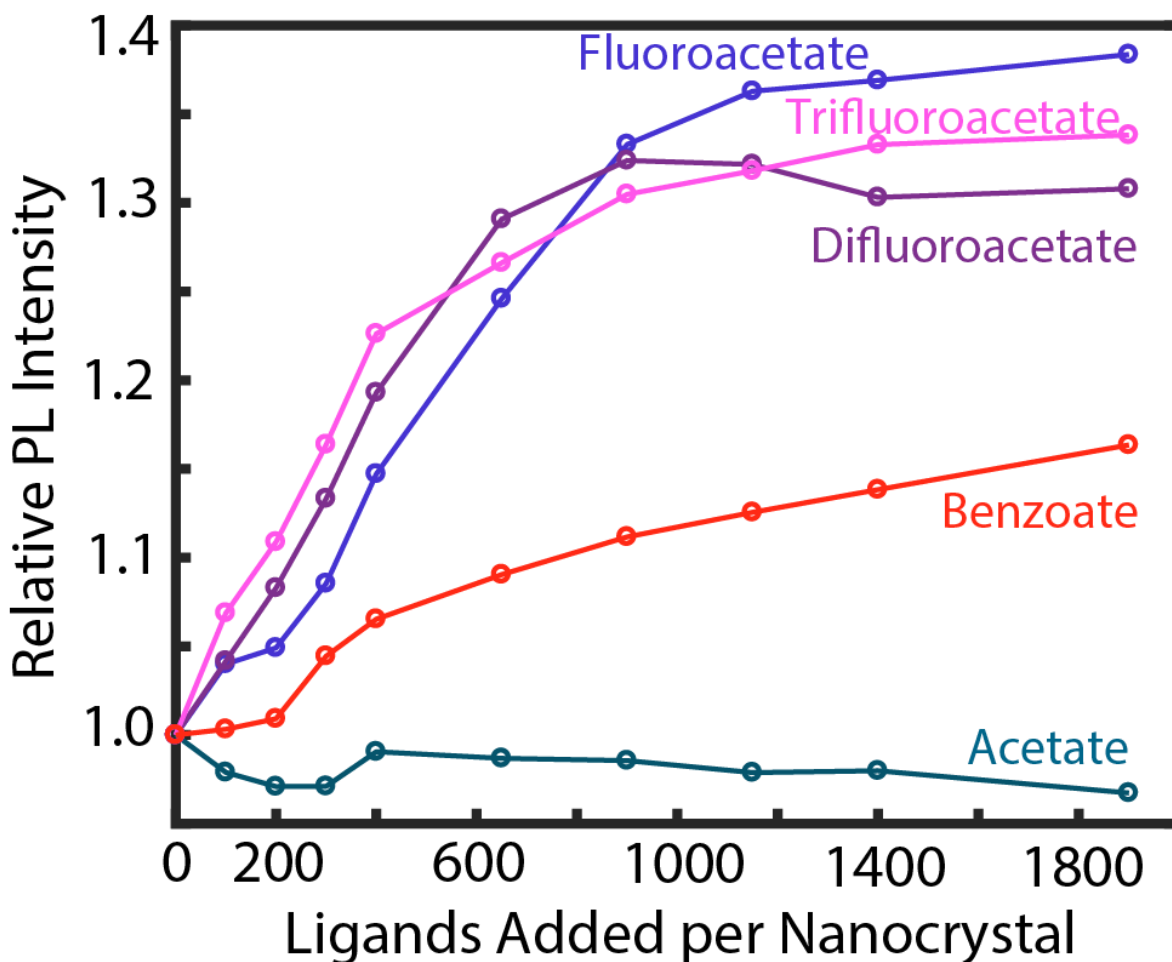


**Figure S23.** Comparison of the effect of carboxylates with variable softness binding heads on CsPbBr<sub>3</sub> nanocrystal PL intensity. All ligand solutions were prepared with oleylammonium as a counterion. Ligand solutions were slowly titrated into cuvettes of dilute CsPbBr<sub>3</sub> nanocrystals, and PL was measured several times after each addition to ensure an equilibrium value. Acetate, the hardest carboxylate in this experiment, has a negligible effect on PL, owing to the unfavorable hard-soft interaction between acetate and Pb. In contrast, benzoate and fluorinated carboxylates significantly improve PL, as these binding heads are softer and thus better suited to bind Pb. No clear trend is observed between the various fluorinated carboxylates. Although benzoate is the softest carboxylate present, the steric hindrance of the aromatic ring hinders its ability to substitute into halide vacancies, and thus PL cannot be improved as significantly as for other softer carboxylates. This highlights the importance of sterics in addition to the hard/soft match with lead.

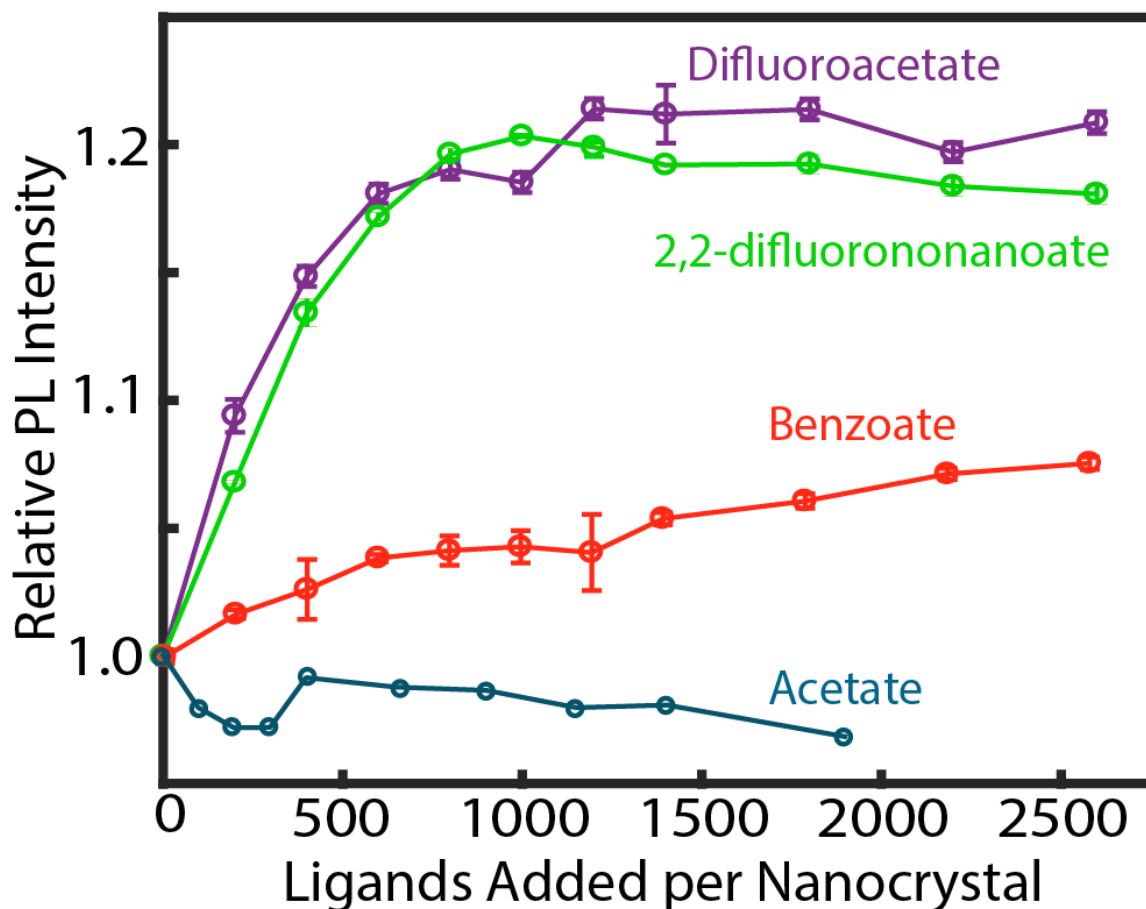


**Figure S24.** Comparison of the effect of carboxylates with variable steric hindrances on CsPbBr<sub>3</sub> nanocrystals relative PL. Given that these ligands are proposed to bond to under-coordinated Pb by substituting into halide vacancies, it is expected that sterics close to the binding head will play a significant role in surface passivation and thus PLQY. This is clearly observed with benzoate – although this is the softest carboxylate in the comparison, the steric bulk of the aromatic ring makes it difficult for this ligand to substitute into halide vacancies. Ligands such as difluoroacetate and 2,2-difluorononanoate have less steric hindrance near the binding head, and thus are more effective for surface passivation. However, as the nanocrystal surface approaches saturation, the long alkyl chain of 2,2-difluorononanoate hinders the efficacy of this ligand, and thus it is not quite as effective as difluoroacetate.

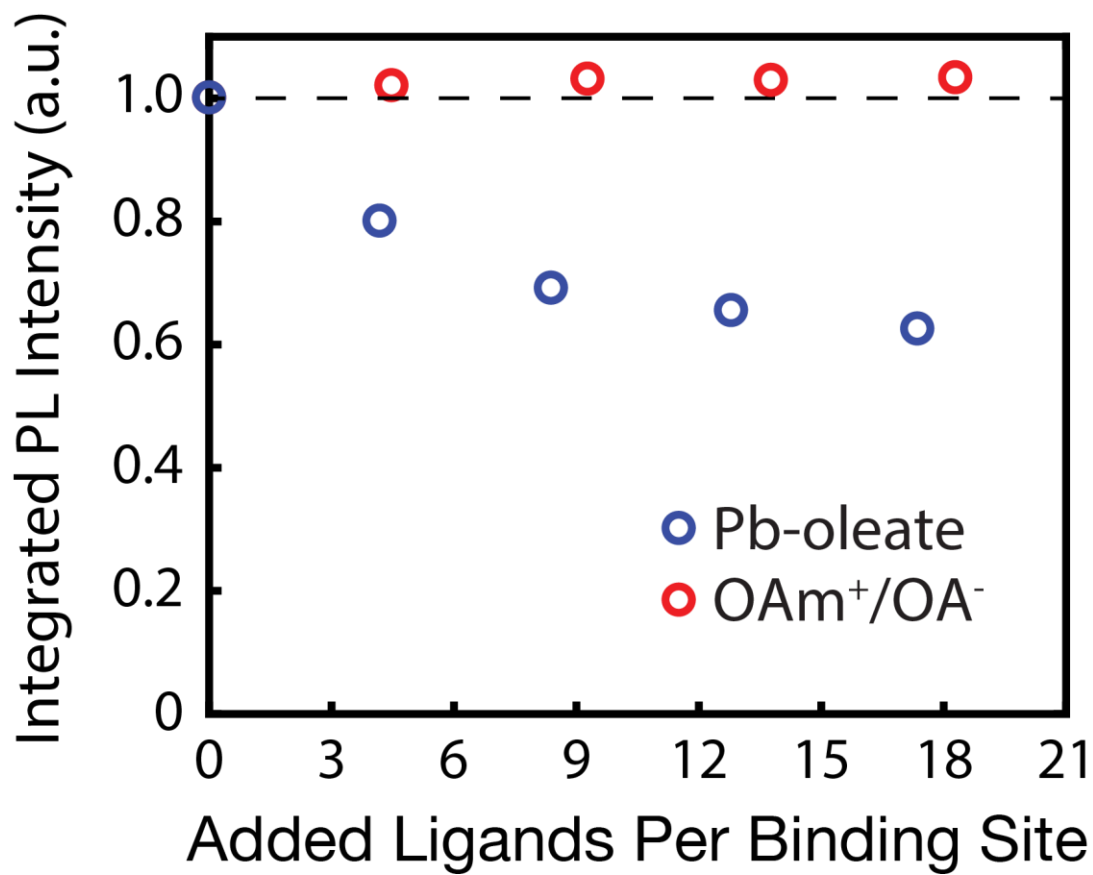


**Figure S25.** PL intensity of CsPbBr<sub>3</sub> nanocrystal samples (concentration 0.019  $\mu$ M) titrated with solutions of lead oleate (blue) or oleylammonium-oleate (OAm<sup>+</sup>-OA<sup>-</sup>). Measurements were repeated several times over the course of hours to ensure no long-term degradation was occurring. Pb-oleate is a Z-type ligand, whereas oleylammonium-oleate is a pair of X-type ligands. Although Z-type ligands have been shown to be important for improving PLQY in metal chalcogenide nanocrystals, here they are observed to have a negative effect on CsPbX<sub>3</sub> nanocrystals. Pb-oleate represents a major byproduct of the synthesis given the Pb-rich conditions, further highlighting the need for a purification method that can remove this byproduct. This also has implications for the anion exchange of CsPbX<sub>3</sub> NCs. Typically, a PbX<sub>2</sub> salt is dissolved by oleylamine and oleic acid in toluene, and this solution is then added to a solution of nanocrystals to initiate the anion exchange. This means that Pb-oleate is present in significant concentrations, thus PLQY is almost certainly being harmed. The pursuit of anion exchange methods free from Pb-oleate, or free of Pb in general, seem like worthwhile pursuits, although using our method, samples can be anion exchanged and then cleaned of all excess exchange solution.

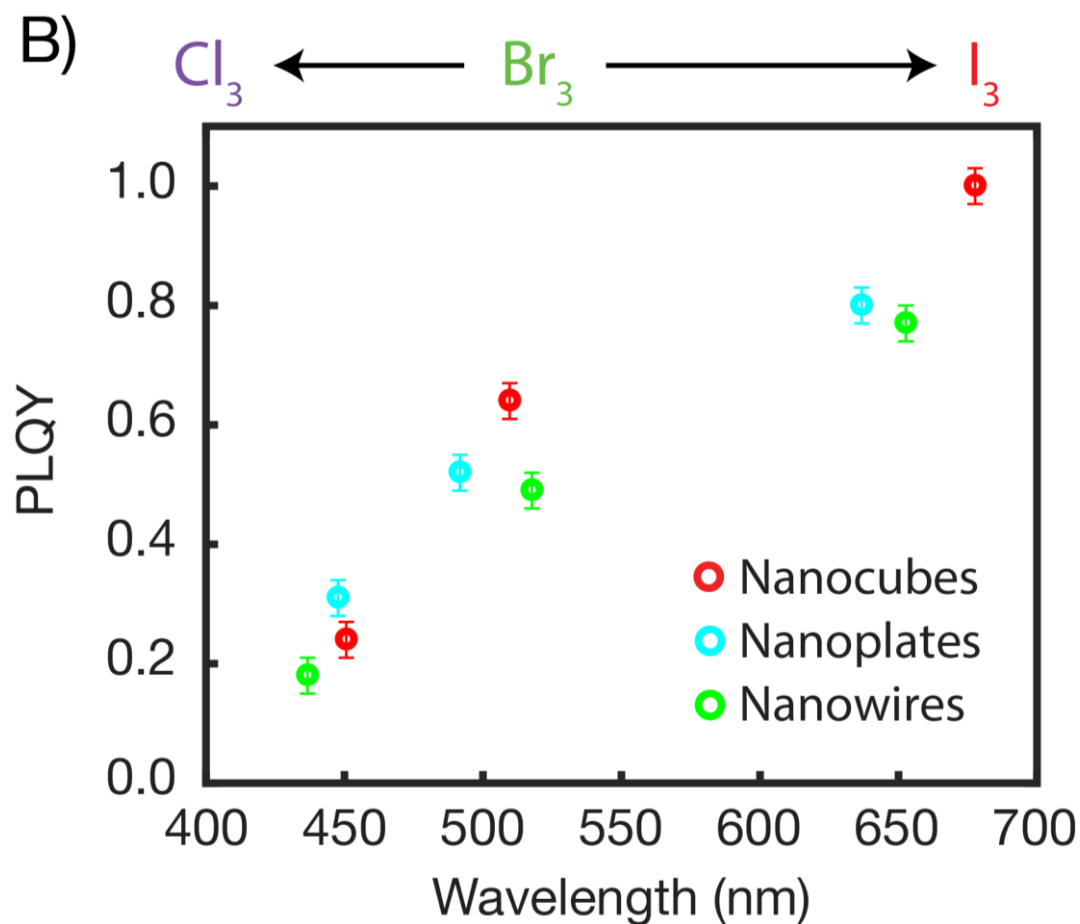


**Figure S26.** Comparison of PLQY as a function of halide composition for  $\text{CsPbX}_3$  nanocubes, nanowires, and nanoplates.  $\text{CsPbBr}_3$  samples were synthesized directly, and then anion exchanged to produce  $\text{CsPbI}_3$  and  $\text{CsPbBr}_{1.5}\text{Cl}_{1.5}$  nanomaterials. Nanowires and nanoplates exhibit the same trends as nanocubes, namely PLQY that is lowest in  $\text{CsPbCl}_3$  and highest in  $\text{CsPbI}_3$ . As such, the general passivation mechanism is expected to readily extend to all morphologies, not just nanocubes.



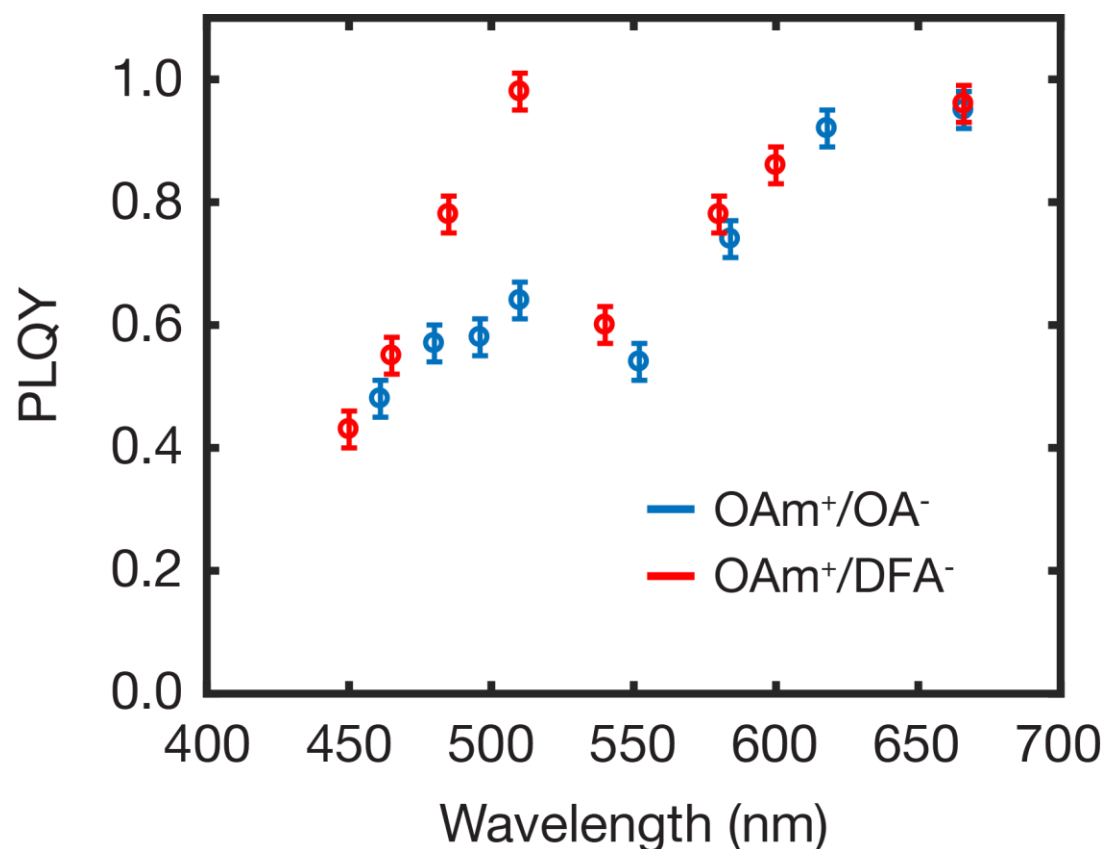


**Figure S27.** PLQY for a variety of halide compositions that are either passivated with oleylammonium-difluoroacetate (red) or purified with oleylammonium-oleate (blue) as a control. Our findings predict that  $\text{CsPbBr}_{3-x}\text{I}_x$  compositions between near-unity PLQY  $\text{CsPbBr}_3$  and near-unity PLQY  $\text{CsPbI}_3$  should also display near-unity PLQY. However, PLQY of  $\text{CsPbBr}_{3-x}\text{I}_x$  nanocrystals is significantly lower than that of  $\text{CsPbBr}_3$  and  $\text{CsPbI}_3$ , with a minimum near  $\text{CsPbBr}_{1.5}\text{I}_{1.5}$ . Additionally, X-type passivating ligands that were effective for  $\text{CsPbBr}_3$  have a negligible effect here. These results can be interpreted in light of a report by Cottingham et al.,<sup>24</sup> who used pair distribution function analysis to demonstrate that  $\text{CsPbBr}_{3-x}\text{I}_x$  nanocrystals phase separate into multiple domains, which is well-known for bulk  $\text{CsPbBr}_{3-x}\text{I}_x$ . Based on the significant decrease in PLQY and the negligible effect of passivating ligands, we hypothesize that deep traps are formed in the interior of the crystal, likely due to grain boundaries or lattice strain. The realization of unity PLQY for this 530-650 nm wavelength range could prove difficult, although further investigation is needed.

In contrast to  $\text{CsPbBr}_{3-x}\text{I}_x$  crystals,  $\text{CsPbBr}_{3-x}\text{Cl}_x$  systems have been demonstrated to form domain-free crystals with halides randomly distributed about Pb centers. As such, these nanocrystals should be effectively passivated with X-type ligand pairs. We found the greatest effect to be on  $\text{CsPbBr}_{3-x}\text{Cl}_x$ , where  $x < 1.5$ . For chloride-dominant alloys, we were unable to significantly improve PLQY. However, this is consistent with the surface model and passivation mechanism we have proposed. As the chloride concentration increases, the lattice contracts and the surface vacancies decrease in size, making it increasingly difficult for an entire binding group to occupy a halide vacancy. As such, we propose that trap-free  $\text{CsPbCl}_3$  nanocrystals are best pursued by small post-synthetic etchants such as thiocyanate and tetrafluoroborate,<sup>25-26</sup> or through improved synthetic protocols.

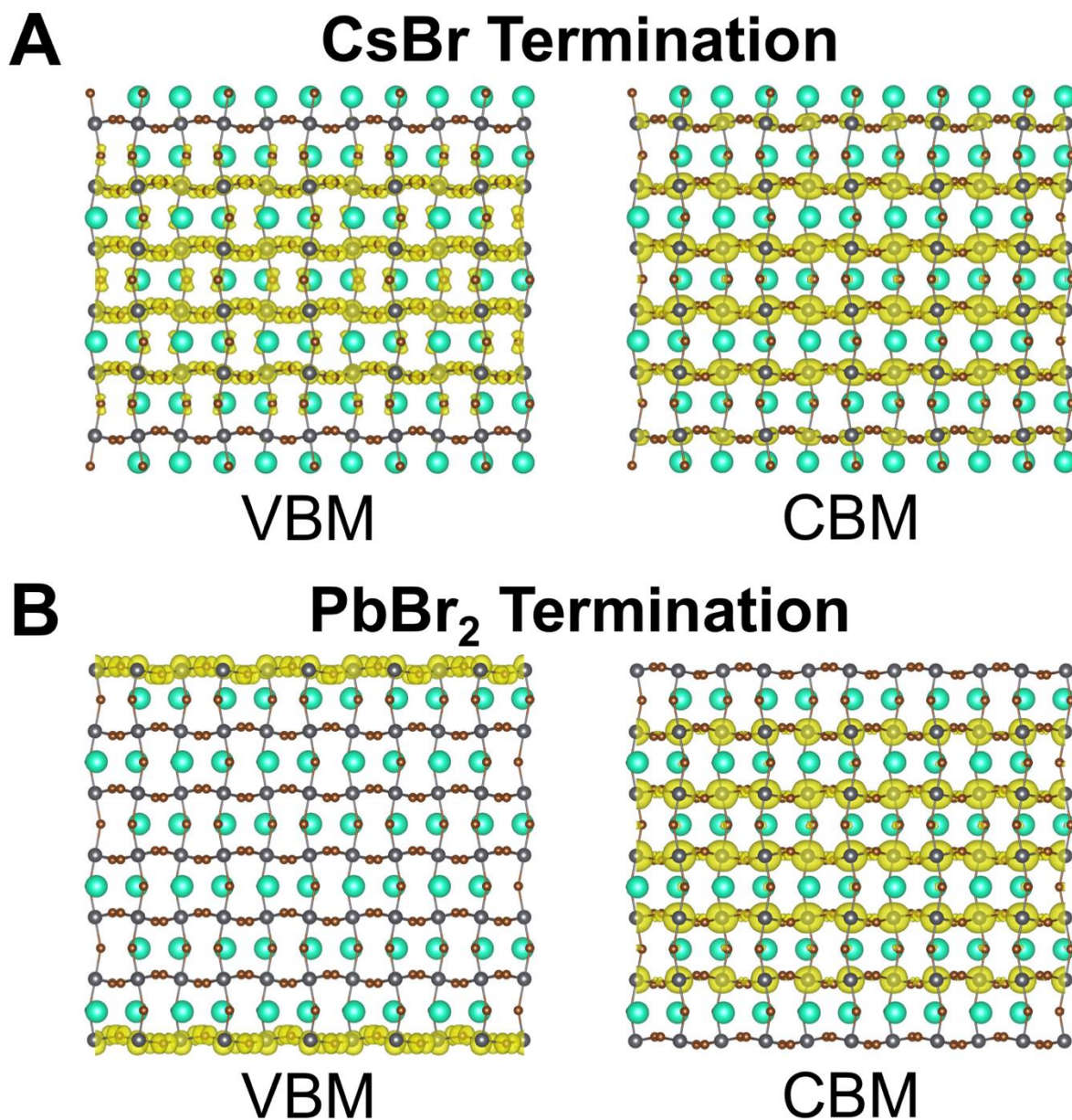


**Figure S28.** Charge density plots of the valence band maximum (VBM) and conduction band minimum (CBM) of (A) CsBr and (B) PbBr<sub>2</sub> surface terminations of CsPbBr<sub>3</sub> crystals. Blue-green atoms are Cs, gray atoms are Pb, and orange atoms are Br. CsBr termination yields a fully delocalized electronic structure that is expected for pristine semiconductor materials, whereas PbBr<sub>2</sub> termination yields a highly localized valence band maximum (VBM) that would introduce significant surface trapping. These results suggest that AX termination is highly beneficial for optoelectronic performance, and thus it is fortunate that these materials tend to spontaneously terminate with these facets.

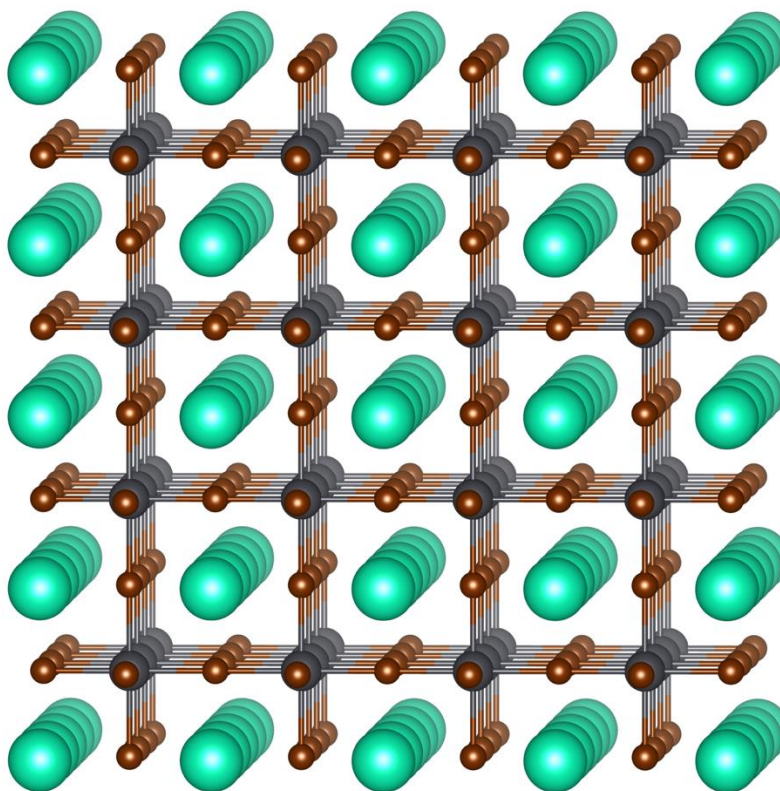


**Figure S29.** View of  $\text{CsPbBr}_3$  crystal lattice with CsBr termination. Blue-green atoms are Cs, gray atoms are Pb, and orange atoms are Br. The enumeration of  $190 \pm 20$  traps per nanocrystal is nearly identical to that of the number of edge and corner atoms ( $188 \pm 10$  per  $9.4 \pm 0.5$  nm nanocrystal), and it is well-known that edge and corner atoms are the most easily removed since they have the fewest neighbor interactions. However, for CsX termination, edges and corners are entirely Cs atoms, thus we conclude that this is simply a coincidence, and halide vacancies are present on the facets of the crystal.

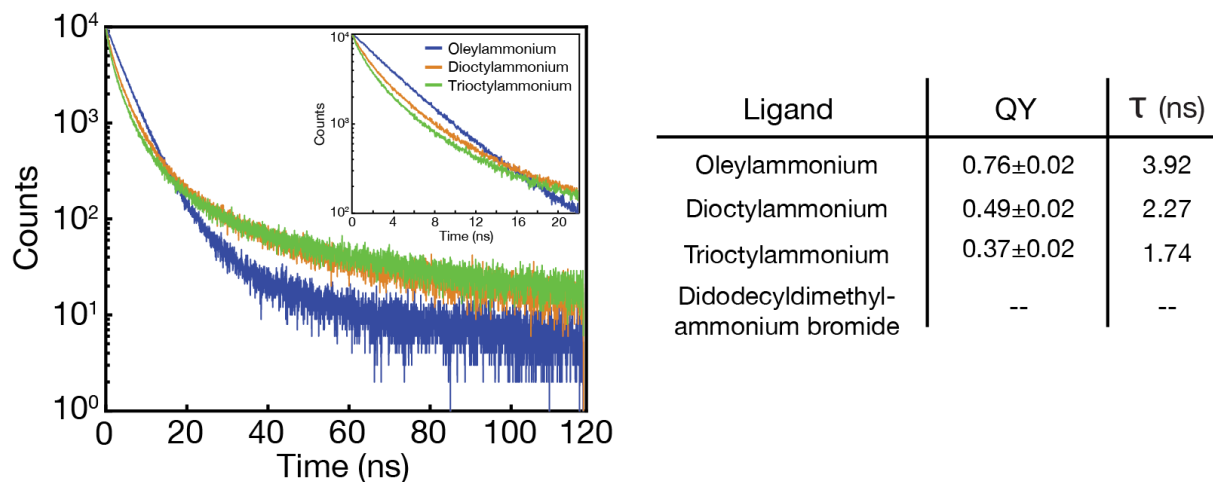


**Figure S30.** Time-resolved photoluminescence lifetimes (Picoquant FluoTime 300) under pulsed 407 nm excitation (10 MHz) at room temperature for CsPbBr<sub>3</sub> nanocrystal samples in toluene capped with identical concentrations of various different ammonium species. Oleic acid was used to form ion pairs since we have now shown several times that it tends not to act as a ligand, and thus the surface will be capped only by the ammonium species of interest here. Primary ammonium species provide the most effective surface passivation, while secondary, tertiary, and quaternary ammonium species are less effective at passivation. This is likely dominated by sterics, as a highly branched ligand such as trioctylammonium would have difficulty packing on the surface. Also worth noting is that although DDAB has been reported in the literature as a way to improve PLQY, DDAB alone cannot act as a ligand. A complete exchange to this ligand yields an off-white precipitate that does not fluoresce, and thus no PLQY or lifetime is reported since the precipitate is no longer in the perovskite phase.



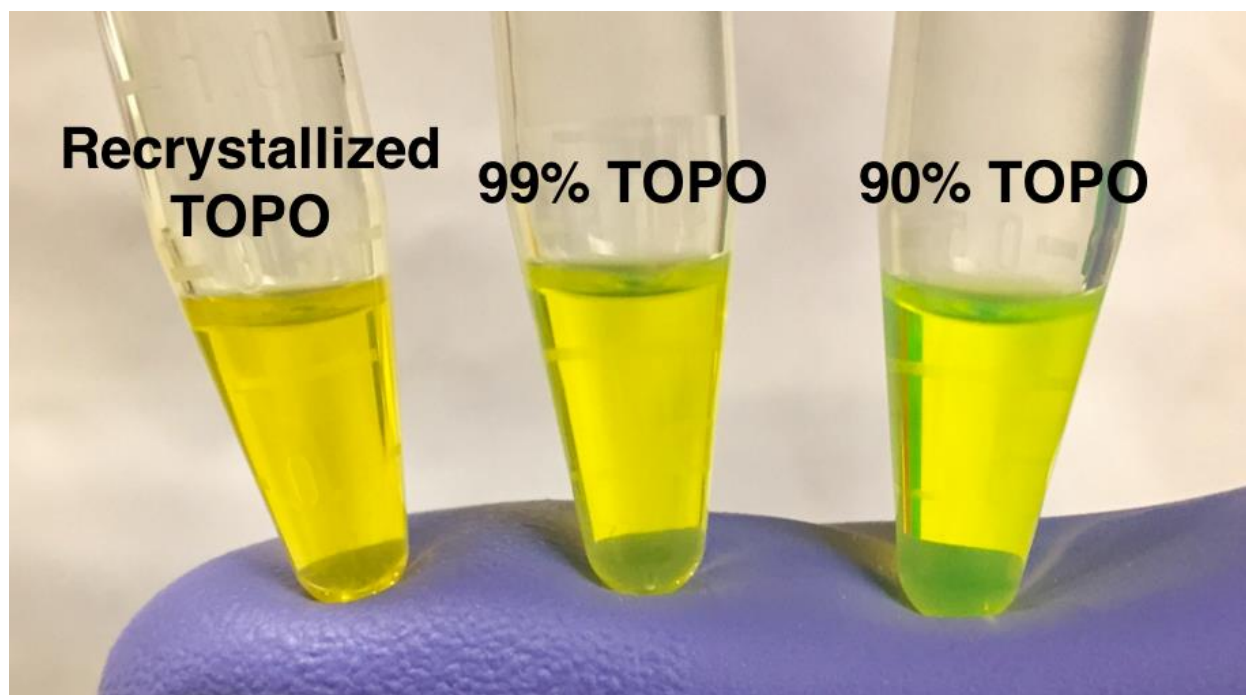


**Figure S31.** Images of the same NC sample 3× exchanged with different purities of trioctylphosphine oxide (TOPO). In light of a recent report about the use of trioctylphosphine oxide (TOPO) as a capping ligand for cesium lead halide perovskite NCs,<sup>27</sup> we find it important to point out that TOPO is known to contain phosphonic acid impurities. This was a point of confusion in early metal-chalcogenide NC literature for many years, and it was discovered that the phosphonic acid impurities, not TOPO itself, was responsible for the desired chemistry. The picture above makes it clear that different purities of TOPO have different effects on the surface chemistry of perovskite NCs. The 90% purity is bright luminescent green due to the relatively high concentration of phosphonic acid impurities that are present (see main text for extended discussion of phosphonate-capped NCs). The 99% purity sample is still fairly luminescent due to impurities, while the recrystallized, high purity TOPO sample is a dim yellow rather than a bright green, indicating that TOPO alone is not effective at passivating the NC surface.

## References

1. Protesescu, L.; Yakunin, S.; Bodnarchuk, M. I.; Krieg, F.; Caputo, R.; Hendon, C. H.; Yang, R. X.; Walsh, A.; Kovalenko, M. V. *Nano Lett.* **2015**, *15*, 3692-3696.
2. Yang, Z. Y.; Burton, D. J. *The Journal of Organic Chemistry* **1992**, *57*, 5144-5149.
3. Bosch, M. P.; Perez, R.; Lahuerta, G.; Hernanz, D.; Camps, F.; Guerrero, A. *Biorg. Med. Chem.* **1996**, *4*, 6.
4. Bronstein, N. D.; Yao, Y.; Xu, L.; O'Brien, E.; Powers, A. S.; Ferry, V. E.; Alivisatos, A. P.; Nuzzo, R. G. *ACS Photonics* **2015**, *2*, 1576-1583.
5. Kresse, G.; Furthmüller, J. *Phys. Rev. B* **1996**, *54*, 11169-11186.
6. Kresse, G.; Joubert, D. *Phys. Rev. B* **1999**, *59*, 1758-1775.
7. Heyd, J.; Scuseria, G. E.; Ernzerhof, M. *J. Chem. Phys.* **2003**, *118*, 8207-8215.
8. Perdew, J. P.; Burke, K.; Ernzerhof, M. *Phys. Rev. Lett.* **1996**, *77*, 3865-3868.
9. Ravi, V. K.; Santra, P. K.; Joshi, N.; Chugh, J.; Singh, S. K.; Rensmo, H.; Ghosh, P.; Nag, A. *J. Phys. Chem. Lett.* **2017**, *8*, 4988-4994.
10. Huang, X.; Paudel, T. R.; Dowben, P. A.; Dong, S.; Tsymbal, E. Y. *Phys. Rev. B* **2016**, *94*, 195309.
11. Uratani, H.; Yamashita, K. *J. Phys. Chem. Lett.* **2017**, *8*, 742-746.
12. Ohmann, R.; Ono, L. K.; Kim, H.-S.; Lin, H.; Lee, M. V.; Li, Y.; Park, N.-G.; Qi, Y. *J. Am. Chem. Soc.* **2015**, *137*, 16049-16054.
13. Dang, Z.; Shamsi, J.; Akkerman, Q. A.; Imran, M.; Bertoni, G.; Brescia, R.; Manna, L. *ACS Omega* **2017**, *2*, 5660-5665.
14. Philippe, B.; Park, B.-W.; Lindblad, R.; Oscarsson, J.; Ahmadi, S.; Johansson, E. M. J.; Rensmo, H. *Chem. Mater.* **2015**, *27*, 1720-1731.
15. Koscher, B. A.; Bronstein, N. D.; Olshansky, J. H.; Bekenstein, Y.; Alivisatos, A. P. *J. Am. Chem. Soc.* **2016**, *138*, 12065-12068.
16. Akkerman, Q. A.; D'Innocenzo, V.; Accornero, S.; Scarpellini, A.; Petrozza, A.; Prato, M.; Manna, L. *J. Am. Chem. Soc.* **2015**, *137*, 10276-10281.
17. Nedelcu, G.; Protesescu, L.; Yakunin, S.; Bodnarchuk, M. I.; Grotevent, M. J.; Kovalenko, M. V. *Nano Lett.* **2015**, *15*, 5635-5640.
18. Maes, J.; Balcaen, L.; Drijvers, E.; Zhao, Q.; De Roo, J.; Vantomme, A.; Vanhaecke, F.; Geiregat, P.; Hens, Z. *J. Phys. Chem. Lett.* **2018**, *9*, 3093-3097.
19. Kleckner, I. R.; Foster, M. P. *Biochim. Biophys. Acta* **2011**, *1814*, 942-968.
20. De Roo, J.; Ibáñez, M.; Geiregat, P.; Nedelcu, G.; Walravens, W.; Maes, J.; Martins, J. C.; Van Driessche, I.; Kovalenko, M. V.; Hens, Z. *ACS Nano* **2016**, *10*, 2071-2081.
21. Liu, Z.; Bekenstein, Y.; Ye, X.; Nguyen, S. C.; Swabeck, J.; Zhang, D.; Lee, S.-T.; Yang, P.; Ma, W.; Alivisatos, A. P. *J. Am. Chem. Soc.* **2017**, *139*, 5309-5312.
22. Udayabhaskararao, T.; Houben, L.; Cohen, H.; Menahem, M.; Pinkas, I.; Avram, L.; Wolf, T.; Teitelboim, A.; Leskes, M.; Yaffe, O.; Oron, D.; Kazes, M. *Chem. Mater.* **2018**, *30*, 84-93.
23. Palazon, F.; Almeida, G.; Akkerman, Q. A.; De Trizio, L.; Dang, Z.; Prato, M.; Manna, L. *Chem. Mater.* **2017**, *29*, 4167-4171.
24. Cottingham, P.; Brutchey, R. L. *Chem. Mater.* **2016**, *28*, 7574-7577.
25. Koscher, B. A.; Swabeck, J. K.; Bronstein, N. D.; Alivisatos, A. P. *J. Am. Chem. Soc.* **2017**, *139*, 6566-6569.
26. Ahmed, T.; Seth, S.; Samanta, A. *Chem. Mater.* **2018**, *30*, 3633-3637.

27. Wu, L.; Zhong, Q.; Yang, D.; Chen, M.; Hu, H.; Pan, Q.; Liu, H.; Cao, M.; Xu, Y.; Sun, B.; Zhang, Q. *Langmuir* **2017**, *33*, 12689-12696.